

# Water Resources Research

## RESEARCH ARTICLE

10.1029/2022WR032716

#### **Key Points:**

- A depth-resolved landslides hydro-mechanical triggering model is provided for dynamically determine the sliding surface of shallow landslides
- The occurrence time, volume, and spatial distribution of shallow landslides are reproduced through the numerical model
- The stability of shallow landslides can be influenced by antecedent rainfall intensity

#### Correspondence to:

X. Hu, huxiaobo@imde.ac.cn

#### Citation:

Jiang, Y., Hu, X., Liang, H., Ning, P., & Fan, X. (2023). A physically based model for the sequential evolution analysis of rainfall-induced shallow landslides in a catchment. *Water Resources Research*, 59, e2022WR032716. https://doi.org/10.1029/2022WR032716

Received 13 SEP 2022 Accepted 17 APR 2023

#### **Author Contributions:**

Conceptualization: Xiaobo Hu, Heng Liang, Po Ning, Xiaoyi Fan Data curation: Xiaobo Hu Formal analysis: Xiaobo Hu Investigation: Xiaobo Hu, Xiaoyi Fan Methodology: Xiaobo Hu Project Administration: Xiaoyi Fan Resources: Xiaobo Hu Software: Xiaobo Hu, Heng Liang, Po Ning Validation: Xiaobo Hu Visualization: Xiaoyi Fan Writing – original draft: Xiaobo Hu

Writing - review & editing: Xiaobo Hu

© 2023. American Geophysical Union. All Rights Reserved.

## A Physically Based Model for the Sequential Evolution Analysis of Rainfall-Induced Shallow Landslides in a Catchment

Yuanjun Jiang<sup>1</sup>, Xiaobo Hu<sup>1,2</sup>, Heng Liang<sup>1</sup>, Po Ning<sup>1</sup>, and Xiaoyi Fan<sup>3</sup>

<sup>1</sup>Key Lab of Mountain Hazards and Surface Processes, Institute of Mountain Hazards and Environment, Chinese Academy of Sciences, Chengdu, China, <sup>2</sup>University of Chinese Academy of Sciences, Beijing, China, <sup>3</sup>School of Civil Engineering and Geomatics, Southwest Petroleum University, Chengdu, China

**Abstract** Predicting the occurrence time, volume, distribution and run-out length of shallow landslides is critical for assessing the volume of debris flow in a catchment. Recent studies suggest that the landslides hydro-mechanical triggering (LHT) model based on threshold-based mechanical interactions can adequately predict rainfall-induced landslides. However, this model assumes that the soil-rock interface is the only sliding surface and cannot dynamically determine a sliding surface above the soil-rock interface. Therefore, by calculating the wetting front depth in the shallow soil layer and using the limit analysis method, the most likely sliding surface can be dynamically calculated to improve the model. Through linking the Soil and Water Assessment Tool (SWAT, USDA) model and the depth-resolved LHT model (D-LHT), a framework for predicting shallow landslides in a catchment was proposed in this work. This framework considers the effects of antecedent rainfall, the mechanical reinforcement of roots, and the spatial distribution of soil properties on slopes. The D-LHT model was applied to the Jiangjia gully in Yunnan, China, to adequately predicted the occurrence time, scale and spatial distribution of shallow landslides. In addition, the present and antecedent rainfall effects on the shallow landslide volume were analyzed. The results showed that the average soil moisture content threshold was determined by antecedent and same-day rainfall, which affect the timing and volume of the shallow landslides. This study provides a new method for predicting shallow landslides. The stability and simplicity of the model make it suitable for early warning systems.

#### 1. Introduction

Debris flows are one of the most common geological disasters in mountainous areas (Iverson, 1997). The materials and water sources of debris flows mainly come from loose materials formed by shallow landslides or river sediment and runoff formed by rainfall. In recent decades, shallow landslides and debris flows have occurred frequently and may be associated with the persistently expanding climatic change in many areas of the world (Bagwari et al., 2021). In China, for instance, during the 10 years from 2010 to 2019, an average of approximately 830 catastrophic debris flow events was reported each year. These disasters seriously affect the safety of the lives and property of people in mountainous areas. Due to the catastrophic damage caused by debris flows, it is beneficial to predict the potential of debris flow occurrence in advance. However, one characteristic of debris flows is the abrupt way they occur, with limited precursory signals (Swanson & Swanston, 1976). The operational prediction of such events remains a very large challenge.

The debris material formed by shallow landslides is one of the main sources of debris flows. Predicting the volume, occurrence time and location of shallow landslides is very important for the analysis of debris flow disasters and has an important influence on the scale of debris flow formation and the severity of the disaster. Previous studies have proposed a variety of empirical or theoretical approaches for predicting shallow landslides and slope instability (e.g., Arnone et al., 2011; Bout et al., 2018; Guo et al., 2020; Shen et al., 2018; Subramanian et al., 2020) and applied them to different shallow landslides or debris flow scenarios. These approaches can be classified into two major categories: statistically based models and physically based models (Bout et al., 2018). The statistically based models consider the relationship between the geomorphological, topographically dependent hydrological parameters (e.g., slope, curvature, rainfall intensity, and vegetation cover) and the likelihood of debris flow occurrence (e.g., Caine, 1980; Crosta, 1998; Guzzetti et al., 2007, 2008; Larsen & Simon, 1993; Terlien, 1998). The statistically based models have the advantages of simple data acquisition, long-term prediction and good large-scale applicability. However, as indicated by recent studies (e.g., Segoni et al., 2018; Zhang

JIANG ET AL.



et al., 2019), they are still limited in terms of case-specific feature descriptions and cannot be applied to address nuanced questions (e.g., root mechanical reinforcement and slope instability caused by changes in matrix suction and pore water pressure) and the dynamics of the shallow landslide triggering process.

The physically based models attempt to link the hydrological process and infinite slope stability analysis, and the factor of safety (FOS, i.e., the ratio between resisting and driving forces) is commonly adopted as an indicator to express the mechanical state of the source soil material and debris flow susceptibility. Therefore, many models (e.g., Arnone et al., 2011; Borga et al., 2002; Burton & Bathurst, 1998; Casadei et al., 2003; Dietrich & Montgomery, 1998; Malet et al., 2005; Moonhyun et al., 2019; Pack et al., 1998; Subramanian et al., 2020; Wu & Sidle, 1995) that combine steady-state shallow underground flow with infinite slope stability analysis have been developed to evaluate the effects of soil moisture dynamics on the occurrence times, rates, volumes and locations of shallow landslide. Iverson (2000) developed a model that couples transient infiltration with infinite slope stability considering the effects of pore pressure on hill-slope stability and applied the Transient Rainfall Infiltration and Grid-Based Regional Slope-Stability Model (TRIGRS) (e.g., Baum et al., 2002; Godt et al., 2008; Morrissey et al., 2008). To account for the different dynamics of surface and subsurface flow, more rigorous models, such as the coupled models combining two or three-dimensional Richards equation solvers and infinite slope stability analysis, have been developed (e.g., Camporese et al., 2010; Rigon et al., 2006; Šimůnek et al., 2016), which often require more computational power. However, the traditional FOS-based model can still be considerably improved; for example, it still cannot reproduce the destruction process of landslides and the force interaction between soil columns (Subramanian et al., 2020).

Lehmann and Or (2012) embedded mechanical thresholds resembling concepts of self-organized criticality (SOC) into a hydro-mechanical framework, which simulated a landslide caused by rainfall on a hillslope composed of many interacting soil pillars, and successfully realized the progressive failure process of hillside soil pillars. As described in the SOC framework (Bak et al., 1988), a critical state can be reached through the interaction of load or mass redistribution among many elements and is often used to simulate various sudden large-scale release phenomena, such as large-scale glacier disintegration and landslides (e.g., Faillettaz et al., 2011; Hergarten & Neugebauer, 2000; Piegari et al., 2006). In their study, after soil base failure, failure of mechanical bonds interconnecting soil columns may cascade and trigger an abrupt release of landslides. Due to the computational burden of modeling for large systems, the model of Lehmann and Or (2012) is limited to small slopes. Then, Von Ruette et al. (2013, 2014) extended a simplified version of the landslide hydro-mechanical triggering model of Lehmann and Or (2012) to larger scales encompassing an entire catchment. Fan et al. (2015, 2020) further improved the LHT model by constructing a physics-based load redistribution rule and combining it with the model of Perla et al. (1980) to build a general landslide-debris flow assessment model (Fan, Lehmann, Mcardell, & Or, 2017) and analyzed the effects of the temporal patterns of rainfall intensity and antecedent soil mechanical damage on shallow landslide triggering.

However, the above models based on LHT are established for shallow landslides, assuming that the damage surface of the soil is on the bedrock. Obviously, this limits the scope of application of the LHT model. There are many cases, such as the debris flow in the Jiangjia gully watershed (Hu et al., 2011), showing that the failure surface of the slope soil is not located at the position of the bedrock. The soil layer of the Jiangjia gully watershed is relatively thick, and there has never been a recorded shallow landslide with a slip surface at the bedrock interface. Field surveys and long-term monitoring results show that the soil instability in the Jiangjia gully watershed is mainly manifested in the weathering and spalling of loose materials on the ground caused by rainfall and that the sliding surface is not at the rock-soil interface (Hu et al., 2011; Wang et al., 2009). The LHT model applies well to shallow landslides where the slip surface is at the bedrock interface (Fan et al., 2016; Fan, Lehmann, & Or, 2017). However, this model cannot be directly applied to slope soil instability like that of the Jiangjia gully watershed type. Therefore, it is necessary to further develop this type of model. At present, some search methods or algorithms of the landslide sliding surface have been developed (Chen et al., 2019). Based on infinite slope stability model, Formetta et al. (2016) calculated landslide depth by examining each potential slip surface. Lu et al. (2012) and Chen et al. (2020) proposed a local FOS method to determine sliding surface, which does not assume any shape for the sliding surface. Recently, Bellugi, Milledge, Dietrich, McKean, et al. (2015), Bellugi, Milledge, Dietrich, Perron, et al. (2015) and Bellugi et al. (2021) proposed a new approach that combines multidimensional slope stability model with a deterministic graph-theoretic landslide search algorithm.

In this paper, based on the LHT model, the limit analysis method was employed to search for the sliding surface of a single soil column, and a depth-resolved model that can dynamically determine a sliding surface was proposed. Then, the D-LHT model was combined with the SWAT model to establish a new model to predict shallow

JIANG ET AL. 2 of 25



landslides for both long-term and large-scale watershed landslide prediction. This paper is organized as follows. First, in Section 2, the coupling model strategy is briefly introduced, including the hydrological model and slope failure model, and detailed explanations of the implemented equations are provided. A classic SWAT model was employed (e.g., Maharjan et al., 2013; Mehan et al., 2017) to simulate the slope water collection and seepage process caused by rainfall, which considers the detailed regulation of vegetation on the hydrological process and provides time-series data of the runoff and seepage flow of the slope for the subsequent stability model. Second, in Section 3, the acquisition and source of model parameter information are introduced, and the sensitivity of the parameters is analyzed, which improves the simulation accuracy of the model. Then, in Section 4, the model is verified with the monitoring data of debris flows that broke out in 2009 in the Jiangjia gully. In addition, the limitations of the model and the future improvements are discussed. Finally, in Section 5, the effects of antecedent rainfall and root strength on shallow landslides are discussed.

## 2. Numerical Modeling Strategy

In this study, a hydrological model was combined with a physical slope model to simulate the instability of rainfall-induced slope movements. The movement of the hydrological slope was modeled through the hydrological module in the open-source program SWAT model, considering the hydrological processes such as rainfall infiltration, runoff from slopes, vegetation interception, and evapotranspiration in detail. First, the SWAT model was used to calculate the spatial distribution of the soil moisture content and runoff depth at different times in the study area. Then, the calculated soil moisture content and runoff depth were imported into the slope stability model to predict the spatiotemporal stability of shallow landslides.

The physical slope stability model proposed in this paper refers to the concept of the LHT model (e.g., Lehmann & Or, 2012; von Ruette et al., 2013), which uses the concept of SOC to describe material failure. The D-LHT model retains the load redistribution, root reinforcement, soil column failure threshold features of the LHT model, and is modified as follows: (a) The slip surface is not limited to the soil-bedrock interface, and it is assumed that there are multiple potential sliding surfaces in the depth direction (including the soil-bedrock interface). The depth of the wetting front in the soil layer is calculated, and iterative calculation is used to find the most unfavorable sliding surface. (b) The SWAT model is used to simulate the hydrological process of the slope, which considers hydrological effects such as vegetation evapotranspiration, canopy interception, and transpiration. (c) The model considers that vegetation enhances the shear and tensile strength of the soil to different degrees at different depths. The integrated model simulates the rainfall-triggered source soil material instability of debris flows, accounting for the spatial and temporal hydrological dynamics that influence slope failure. A flow chart of the model is shown in Figure 1.

### 2.1. Hydrological Process

SWAT (USDA) is an open source, semi-distributed, semi-physical watershed model that has been widely used in continuous time series hydrological process simulation. The SWAT model divides a research basin into several sub-basins, and includes meteorological information, hydrological response units (HRUs, the smallest hydrological calculation unit in the model, combining a unique land use type, soil type and slope type), groundwater, river courses, and so on (Arnold et al., 2012). First, the various types of discharges are calculated on the hydrological response unit scale. Then the discharges are summarized at the sub-basin level and finally flow through the river channel to the water outlet of the basin. The entire water circulation system follows the water balance law, and the equation is expressed as:

$$sw_t = sw_0 + \sum_{i=1}^{i} (R - Q_{surf} - E_a - w_{seep} - Q_{gw})$$
 (1)

where  $sw_t$  denotes the end water content of a time step (mm),  $sw_0$  is the soil moisture content at the previous integration time step (mm), t represent the time step, R is the total precipitation in step i (mm),  $Q_{surf}$  denotes the total surface runoff in step i (mm),  $E_a$  and  $w_{seep}$  represent the water volume lost via evapotranspiration and seepage in step i (mm), and  $Q_{gw}$  is the total underground water in step i (mm). More details of the hydrological model are described in Appendix A.

### 2.2. Slope Soil Material Stability Modeling

This slope stability model divides the slope soil material of the watershed into an assembly of regular hexagonal-shaped soil columns interconnected by mechanical bonds (like the spring-block models) (Lehmann &

JIANG ET AL. 3 of 25

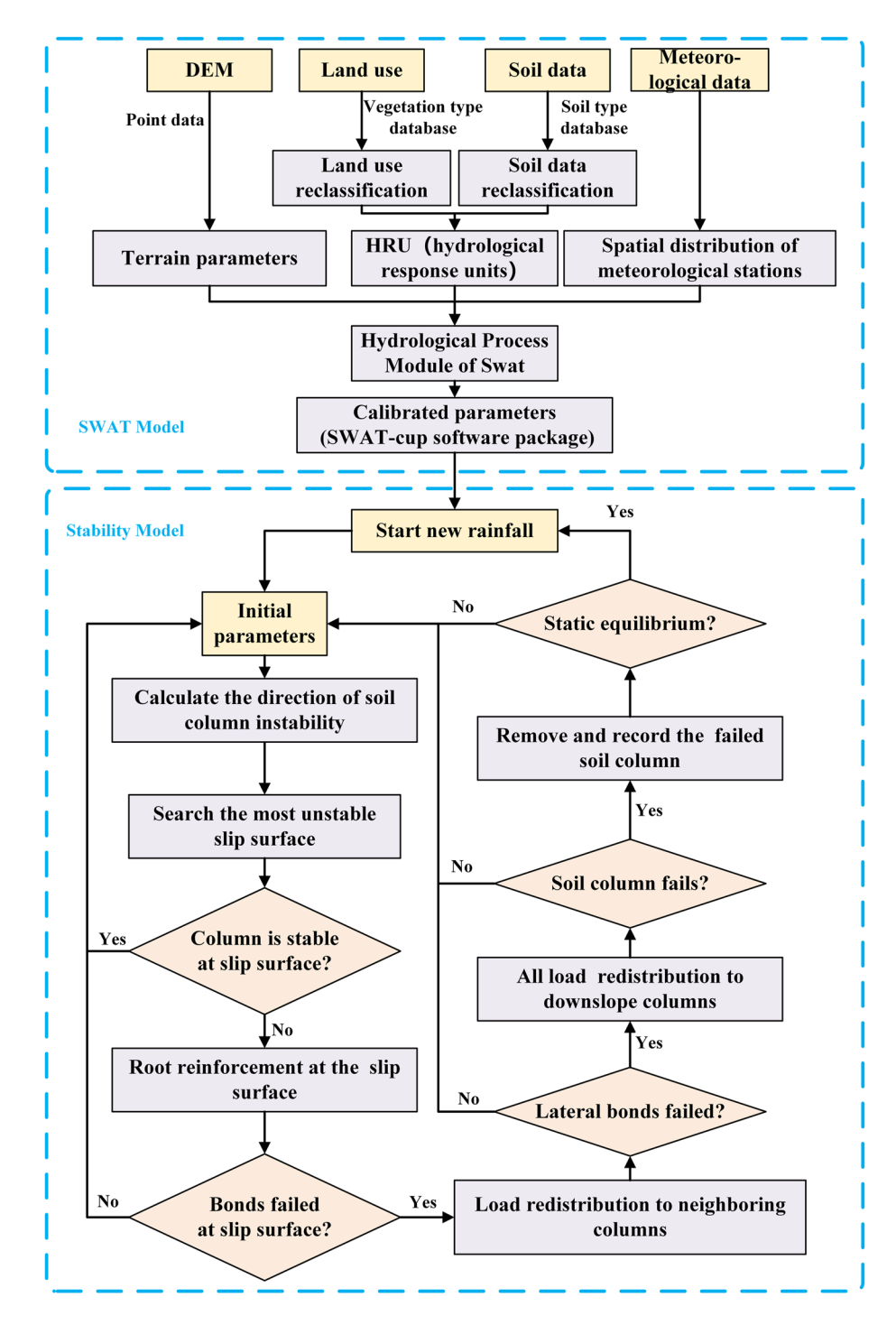


**Figure 1.** Numerical model strategy and flowchart. First, the basic parameters (such as the rainfall intensity, DEM elevation and soil parameters), were input Soil and Water Assessment Tool model to calculate soil moisture content and surface runoff during each time step. Then, the soil moisture content and surface runoff are input into the D-LHT model to calculate the failure process of the soil column.

Or, 2012), as shown in Figure 2. Each hexagonal column has the same distance from the adjacent grid and has isotropic geometric characteristics.

In this model, the limit analysis method is used to iteratively calculate the most unfavorable sliding surface of the soil column (in Section 2.2.4) and consider the influence of hydrology and vegetation on soil mechanical

JIANG ET AL. 4 of 25

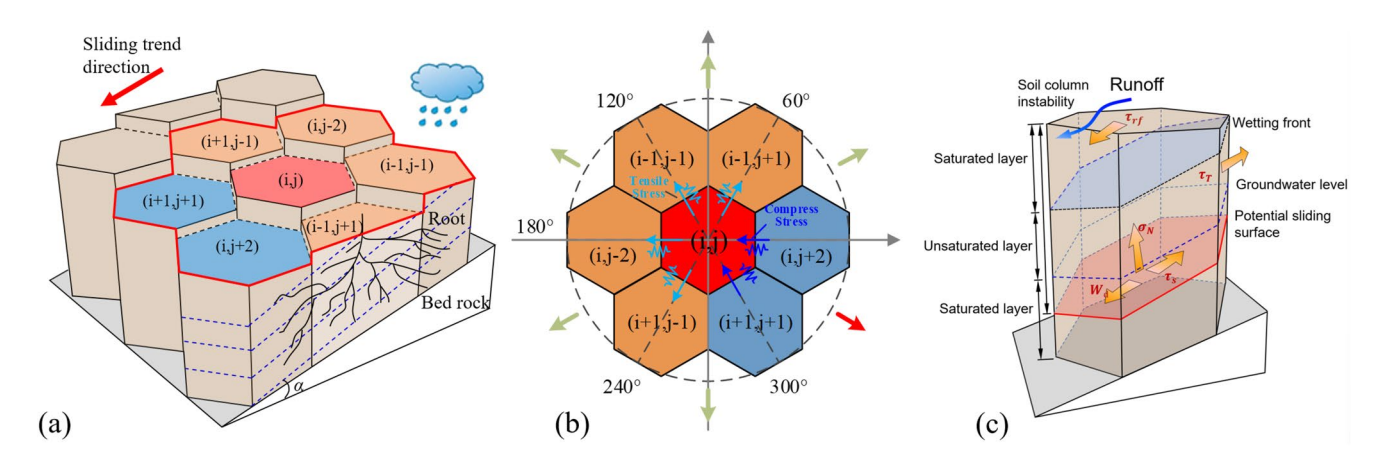


Figure 2. (a) The slope is discretized into hexagonal soil pillars, and each soil pillar is layered in depth; (b) Schematic diagram of the stress action between soil pillars. Along the failure direction of the soil columns (red), the uphill soil columns (orange) and the soil columns on both sides are subjected to tensile stress provided by the roots, while the downhill soil columns (blue) are subjected to compressive stress. (c) Conceptual illustration of the stress on a single soil column. The model can be divided into three horizontal layers according to the saturation state of the soil, and the following situations may arise: (i) All three layers are unsaturated. (iii) The upper and middle layers are unsaturated, and the lower layer is saturated. (iv) The upper layer is saturated, and the middle and lower layers are unsaturated. (v) The upper and lower layers are saturated, and the middle layer is unsaturated in panel (c).

behavior. In the event of rainfall, seepage water gradually changes the weight and strength of the soil column, thereby affecting the change in the sliding surface of the soil column. On different sliding surfaces, the shear strength of vegetation to soil is different.

#### 2.2.1. Depth of the Wetting Front

The wetting front is the interface between the wet soil layer and the dry soil layer formed by the upper soil body becoming wet due to rainfall infiltration. The wetting front divides the soil into an upper humid area and a lower non-humid area. The humid area may reduce the suction of the soil matrix, thereby reducing the shear strength of the soil. The formula proposed by Mein-Larson is used to calculate the depth of the wetting front. The model assumes that the initial soil moisture content and the soil moisture content in moist areas during rainfall infiltration are evenly distributed and the wet part is saturated (Mein & Larson, 1973). This assumption may increase the probability of landslides, leading to an increase in the landslide volume, so the simulation results are conservative (L. Chen & Young, 2006). The model is simple and proven to be effective. The formula of the wetting front is as follows:

$$Z_d = \frac{I}{(\theta_s - \theta_i)\cos\alpha} \tag{2}$$

where  $Z_d$  is the depth of the wetting front (mm), I is the total infiltration of water (mm),  $I = \text{sw}_t - \text{sw}_0$ ,  $\theta_s$  is the maximum volumetric water content (m<sup>3</sup>/m<sup>3</sup>), and  $\theta_i$  is the volumetric soil water content at the previous integration time step (m<sup>3</sup>/m<sup>3</sup>).

#### 2.2.2. Force Evolution of Single Soil Columns

A local FOS-like estimate is used to assess the mechanical conditions and is applied to each individual column. The total sliding force  $W_d$  of the soil column on the slip surface is defined as follows:

$$W_d = W - \tau_T + \tau_{\rm rf} \tag{3}$$

where  $\tau_T$  is the stress from the upslope columns or downslope columns when the soil column is unstable (in Section 2.2.4). The total mass M of a soil column and the downslope force component W of the soil column on the slip interface are given as:

$$W = \frac{Mg\sin\alpha}{A_H/\cos\alpha} = H_d[\theta\gamma_w + (1-\psi)\gamma_r]\sin\alpha\cos\alpha$$
 (4)

where g is acceleration due to gravity,  $A_H$  denotes the hexagonal cross-section of a soil column,  $H_d$  represents the distance from the sliding interface to the ground surface (explained in detail in Section 2.2.4),  $\theta$  is the volumetric water content,  $\psi$  is the porosity, and  $\gamma_w$  and  $\gamma_r$  are the bulk densities of the water and soil minerals, respectively.

JIANG ET AL. 5 of 25



 $\tau_{\rm rf}$  is the shear stress of slope runoff and can be expressed as follows:

$$\tau_{\rm rf} = \gamma_w H_{\rm pond} S_f \tag{5}$$

where  $S_f$  is the slope of the soil column (mm/mm) and  $H_{pond}$  is the depth of runoff (mm), which is calculated by the SWAT model.

The shear stress  $\tau_s$  is a function of the soil column normal stress  $\sigma_n$  and the weakening or reinforcing effects of the soil water and cohesion  $c_{\rm soil}$ . According to Iverson et al. (2000) and Vanapalli et al. (1996), increasing soil water results in an increase in pore water pressure, modifying the soil internal strength and reducing the effective stress of the soil. That is, when rainfall infiltrates the slope soil, as the soil saturation gradually increases, the matrix suction gradually disappears, the pore water pressure gradually increases, or the groundwater level rises, thus reducing the shear strength of the soil. When the soil is in different saturation states (saturated and unsaturated), different formulas need to be used to calculate the shear strength of the soil. The soil saturation state is closely associated with rainfall, soil infiltration properties, and groundwater level etc. The schematic diagram of the soil saturation state is shown in Figure 2c. The calculation formula of  $\tau_s$  is as follows:

$$\tau_{s} = c_{\text{soil}} + (\sigma_{n} + \tau_{h}) \tan \varphi$$

$$+ \tau_{\text{rs,z}} = \begin{cases} c_{\text{soil}} + c_{\text{root}} + \left\{ H_{\text{sd}} [\theta \gamma_{w} + (1 - \psi) \gamma_{r}] \cos^{2} \alpha - h_{s} \gamma_{w} \cos^{2} \alpha \right\} \tan \varphi &, \text{Saturation} \\ c_{\text{soil}} + c_{\text{root}} + \left\{ H_{\text{sd}} [\theta \gamma_{w} + (1 - \psi) \gamma_{r}] \cos^{2} \alpha - \Theta h \gamma_{w} \right\} \tan \varphi &, \text{Unsaturation} \end{cases}$$
(6)

where  $\Theta$  is the effective water saturation,  $\lambda$  is the pore size distribution parameter,  $\tau_h$  is the shear strength as introduced by Bishop (1960), h is the capillary pressure head,  $h_s$  is the height of the free water table in the soil column, and  $\tau_{rs,z}$  is the shear strength (as a function of depth) provided by roots. To incorporate the soil type information into the hydraulic landslide model, Lehmann and Or (2012) and Fan et al. (2015) used the pore size distribution parameter  $\lambda$  of the Brooks and Corey soil water retention model to describe the effect of soil type (soil texture level) on soil hydraulic properties. It has been proven that the inlet value and saturated hydraulic conductivity of the hydraulic function can be expressed as a function of the parameter  $\lambda$  (Lehmann & Or, 2012).

Brooks and Corey (1964) used the model to parameterize the hydraulic properties:

$$\Theta = \left(\frac{\theta - \theta_r}{\theta_s - \theta_r}\right) \begin{cases} \Theta = \left(\frac{h_b}{h}\right)^{\lambda} &, |h| \ge |h_b| \\ \Theta = 1 &, |h| < |h_b| \end{cases}$$
(7a)

$$h = -|h_b|\Theta^{-1/\lambda} \tag{7b}$$

where  $\theta$  is the water content,  $h_b$  is the air-entry value, and  $\theta_r$  and  $\theta_s$  are the residual and maximum water contents, respectively. In Section 4.2, the possible values of  $\lambda$  are described in detail.

#### 2.2.3. Tensile and Compressive Effects of Neighboring Columns

The load of a failed soil column is redistributed to neighboring columns via mechanical bonds. As shown in Figure 2, when the central soil column slides along the sliding surface, it is blocked by the surrounding soil columns, and its excess sliding stress is transferred to the surrounding soil columns. Along the failure direction of the soil columns, the uphill soil columns and the soil columns on both sides are subjected to tensile stress, while the downhill soil columns are subjected to compressive stress. When  $W_d < \sigma_n \tan \varphi$ , the column remains stable under the support of cohesion and soil strength. When  $\sigma_n \tan \varphi < W_d$ , the soil column distributes excess stress to the adjacent soil columns. The formula for the load redistribution to lateral column stress after basal failure is as follows (Lehmann & Or, 2012):

$$\tau_T = \frac{A_H}{A_i \cos \alpha} (W_d - \sigma_n \tan \varphi - \tau_R)$$
 (8)

where  $A_H$  is the area of a soil column with a hexagonal cross-section,  $A_i$  is the intersection area between the two adjacent columns failure planes, and  $\tau_R$  is the residual soil strength after failure at the sliding surface.

It is evident that the topography determines the failure direction of the soil column and thereby the method (tensile or compressive) of the stress transmission of the soil column. Slope instability led to topographical changes, and

JIANG ET AL. 6 of 25



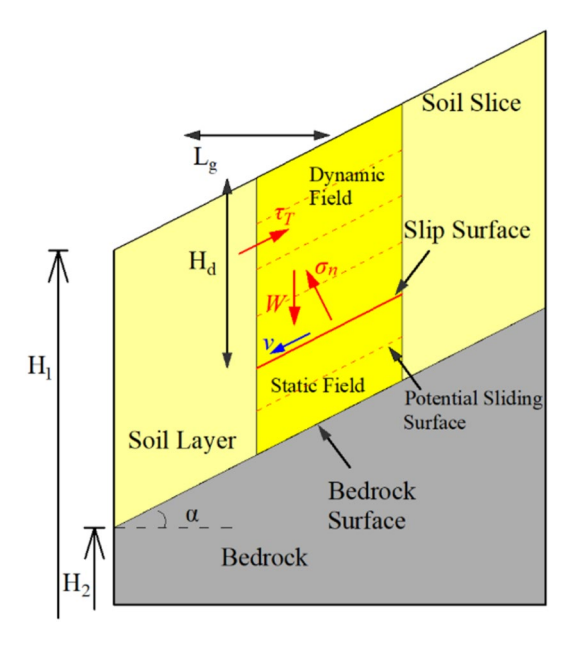


**Figure 3.** Infinite slope model for a variably saturated infinite slope with a weathered mantle. The red solid line is the most dangerous sliding surface and the red dashed lines are the potential sliding surfaces.

the inclination direction of soil column destruction changes accordingly. To simplify the stress transfer of the soil column, let us suppose that the central soil column can only slide in the specified six directions (the stress transfer is symmetrical). According to the least action principle, the central soil column is more inclined to apply compressive stress to the adjacent soil column with lower potential energy if it is unstable. Therefore, the method of Appendix B is adopted to judge the direction of instability and failure of the soil columns.

#### 2.2.4. Soil Column Failure

When the lateral tensile bonds (between the uphill and lateral columns) are all broken, the soil column must be stabilized by the downhill columns. However, when the compressive load imposed on the soil column exceeds its intrinsic compressive strength, the soil column is destroyed and released as a landslide (becomes "fluidized") (e.g., Hu et al., 2011; Lehmann & Or, 2012). The soil fails when the external loads transmitted to the soil exceeds the soil stress limit threshold, which is determined by the nature and structure of the soil. The compressive strength is usually defined as (e.g., Goodman, 1980; Mullins & Panayiotopoulos, 1984):

$$\tau_c = \frac{\sum_{I} N_I}{\sum_{I} A_I} = \frac{2c_{\text{soil}} \cos(\varphi)}{1 - \sin(\varphi)} + \frac{2\sin(\varphi) * \Theta * h}{1 - \sin(\varphi)} \gamma_w \tag{9}$$

where  $N_I$  and  $A_I$  are the compressive load and area acting on the column, respectively.

#### 2.2.5. Distance From the Sliding Surface to the Ground Surface

Based on Equations 2–7, the stress on the soil column in various phases was calculated, but the depth of the sliding surfaces  $H_d$  must be known. Different from the LHT model, this model assumed that any plane parallel to the bedrock surface may be a potential sliding surface. At the same time, the soil column may have only one most dangerous sliding surface. At different depths, the sliding force, shear resistance, and compressive strength of the soil are different (Lu & Godt, 2008). As the depth change, the force  $\tau_T$  from adjacent soil pillars changes with the contact area between adjacent soil pillars. Therefore, the FOS on the potential sliding surface of each soil column (in Figure 3) is calculated. The sliding surface with the smallest FOS is the most dangerous sliding surface. The factor of safety FOS can be denoted as follows:

$$FOS = \frac{\tau_s}{W_d} = \frac{H_d[\theta \gamma_w + (1 - \psi)\gamma_r] \sin \alpha \cos \alpha - \tau_T + \tau_{rf}}{c_{\text{soil}} + (\sigma_n + \tau_h) \tan \varphi + \tau_{\text{rs},z}}$$
(10)

#### 2.2.6. Sensitivity Analysis of the Stability Model

The sensitivity analysis of parameters can help us more efficiently obtain high-confidence simulation results when it is difficult to obtain complete parameters in the study area. Thus, a sensitivity analysis is conducted on the parameters required by the model (Equations 2–9) to calculate the FOS, to determine the impacts of input parameters on the value of the safety factor and to obtain the key input parameters. In the univariate sensitivity analysis of the stability model, all initial parameters are kept constant, except for the parameters chosen for sensitivity analysis (Table 1). Figure 4 shows the effect of each selected parameter change on the FOS. As illustrated in Figure 4, the cohesion and angle of internal friction of the soil are positively correlated with the FOS calculated by the model. While the depth of sliding surface  $H_d$ , Brooks and Corey parameter of the water retention curve  $\lambda$ , volumetric water content  $\theta$  and slope  $\alpha$  are inversely correlated with the FOS. The most sensitive parameters in this model are the Brooks and Corey parameter of the water retention curve  $\lambda$ , volumetric water content  $\theta$  and slope  $\alpha$ , which shows that the inherent mechanical properties of the soil and the topography play the most important role in the stability of the slope. Therefore, the soil geotechnical parameters and digital elevation data in the study area are critical to the accuracy of the simulation.

JIANG ET AL. 7 of 25

<b>Table 1</b> The Parameters of the Univariate Sensitivity Analysis		
Parameters for sensitivity analysis	Initial parameters	Value range of parameters (±30%)
Distance from the sliding interface to the ground surface, $H_d$	1 m	0.6–1.4 m
Volumetric water content, $\theta$	$0.2 \text{ m}^3/\text{m}^3$	$0.12-0.28 \text{ m}^3/\text{m}^3$
Pore size distribution parameter, $\lambda$	0.25	0.15-0.35
Bulk densities of the soil minerals, $\gamma_r$	$1,500 \text{ kg/m}^3$	$900-2,100 \text{ kg/m}^3$
Angle of internal friction, $\varphi$	22°	13.2–30.8°
Soil cohesion, $c_{\text{soil}}$	3,000 Pa	1,800–4,200 Pa
Hill slope, $\alpha$	35°	21–49°

## 3. Overview of the Model and Input Parameters

#### 3.1. Watershed and Meteorological Characteristics

To test the performance of this model, the Jiangjia gully watershed in northeastern Yunnan Province in Southwest China (N  $26^{\circ}13'-26^{\circ}17'$ , E  $103^{\circ}06'-103^{\circ}13'$ ), was selected as the research case. A  $10 \text{ m} \times 10 \text{ m}$  resolution digital elevation model (DEM) shows that the  $48.6 \text{ km}^2$  basin exhibits large elevation changes, rising from 1,062 m to 3,209 m. Based on the data from the debris flow observation station of the Institute of Mountain Hazards and Environment (IMHE) at the Chinese Academy of Sciences, the geological conditions in the area are very active, and the slopes are rich in provenance. From 1965 to 2010, a total of 497 shallow landslides and debris flow events were recorded by the debris flow observation station, with the highest frequency of 28 times a year and an average annual frequency of more than 10; the magnitude of the volume of the flows varies from  $10^3$  to  $10^6$  cubic meters (Guo et al., 2013). Landslides in this basin (Figure 5) mostly occur from June to September, with more than 80% of the total annual rainfall (ranging from 700 to 1,200 mm) occurring in this time (Hu et al., 2011).

#### 3.2. Vegetation Properties and Root Strength

The land use properties required for the modeling are from the global geo-information public product provided by China to the United Nations with a 30-m resolution (http://www.globalland-cover.com/) (Figure 5). In the study area, more than 80% of the area is in the zone 1,500–3,000 m above sea level, namely, mountainous subtropical evergreen broad-leaved forest and mountain temperate coniferous broad-leaved forest mixed forest. There is little forest in the basin, representing 12.3% of the total area of the basin, and grassland accounts for approximately 57.0% of the total area. Cultivated land accounts for approximately 30.4%, and artificial surfaces account for approximately 0.3%.

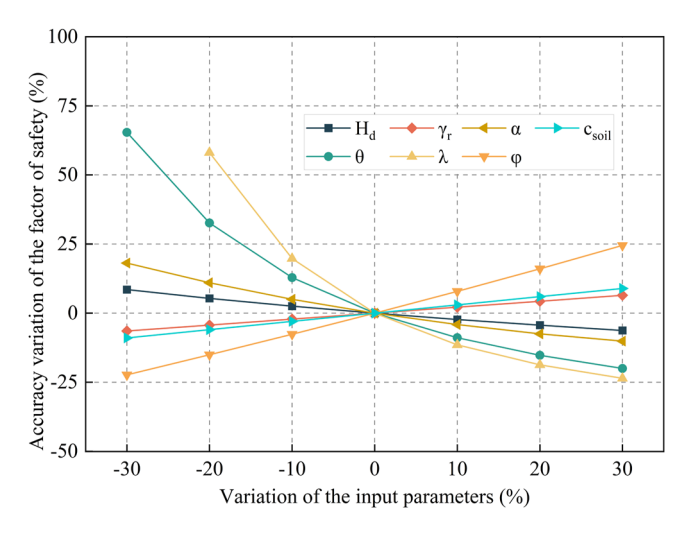


Figure 4. The influence of parameter changes on the FOS.

The main tree species in the forest area in the basin are New albizia julibrissin (NAJ-arbor) and Coriaria sinica (CS-shrub). The roots result in different shear and tensile strengths at different depths. The experimental measurement data of the roots come from a report by Chen et al. (2019). According to Waldron-Wu, based on the Mohr–Coulomb, the root soil shear strength model is established (e.g., Pollen & Simon, 2005; Preti, 2006; Waldron, 1977; Wu et al., 1979; ):

$$\tau_{\text{rs},z} = 1.2 \, K \cdot T_R \cdot A_{\text{RAR}} \tag{11}$$

where K is a dimensionless correction parameter,  $T_R$  is the experimentally measured root tensile strength, and  $A_{\rm RAR}$  is the ratio of the root area and the area with rooted soil. The increment of the root shear strength in soil with depth is shown in Figure 6. The reinforcement depths of the roots of NAJ and CS are approximately 1.6 and 0.8 m, respectively. In addition, due to the limited mechanical reinforcement effect of herbaceous plants on the soil and the sparse growth of herbaceous plants in the study area, the mechanical strengthening effect of the herbaceous plants on the soil is neglected in the simulation.

JIANG ET AL. 8 of 25

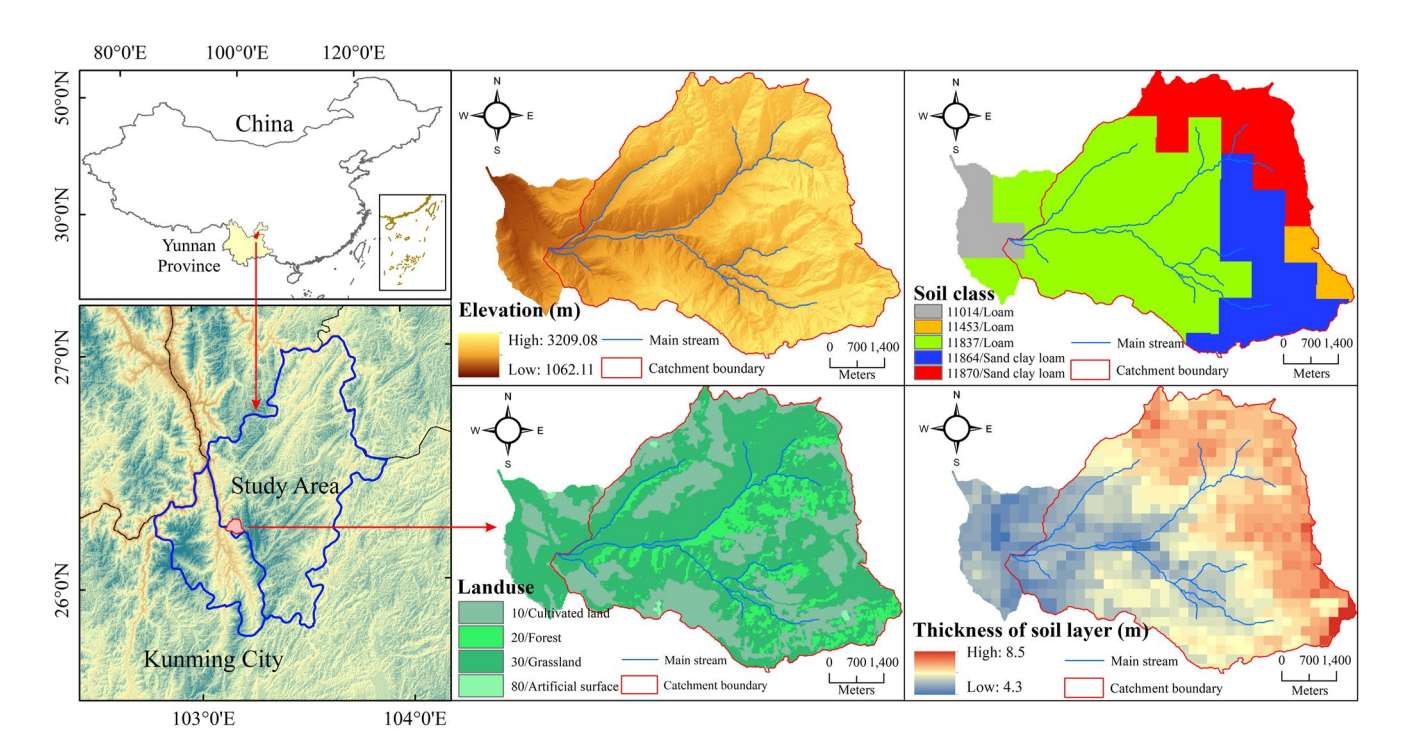


**Figure 5.** Location of the catchment. (a) The yellow area shows the location of Yunnan Province in China, and the red region is the Dongchuan district, Kunming city. (b) The red area is the study area, situated in Kunming city. (c) Digital elevation of the study area. (d) Land use (four types). (e) Soil classes and (f) Thickness of soil layer (Hengl et al., 2017).

## 3.3. Soil Type and Properties

According to the U.S. Department of Agriculture classification system, the soil type and soil hydraulic properties (i.e., soil water retention and hydraulic conductivity) are determined by the fractions of sand, silt and clay minerals. From the soil class diagram (Figure 7), shows 2 types of soil (sandy clay loam and loam) of soil in the basin. The soil classes required for the model are from the website of the Food and Agriculture Organization of the United Nations, with a 250-m resolution (http://www.fao.org/soils-portal/soil-survey/soil-maps-and-databases/harmonized-world-soil-database-v12/en/). The soil texture was mainly classified as loam and sandy clay loam (Figure 7). This is consistent with the field sampling survey value of Hu et al. (2011).

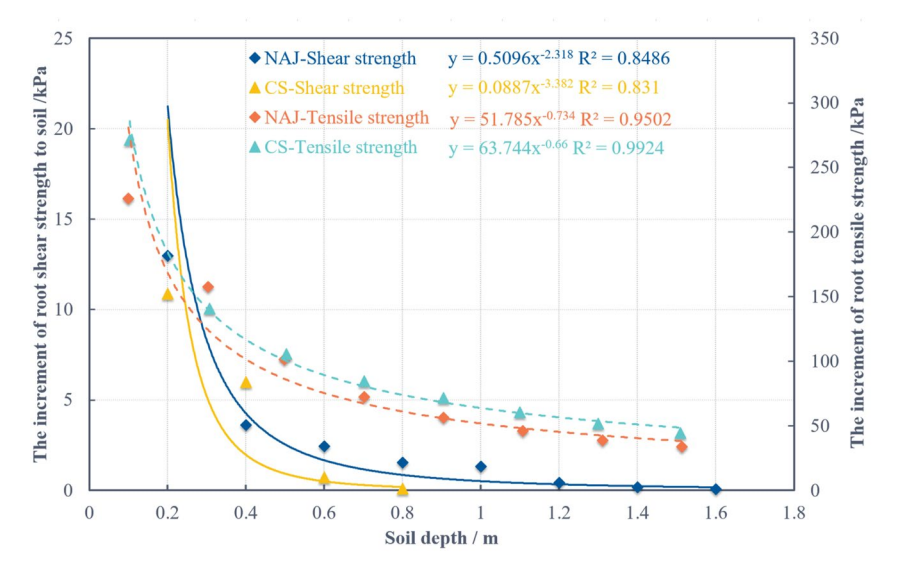


Figure 6. Root shear strength and tensile strength at different depths.

JIANG ET AL. 9 of 25

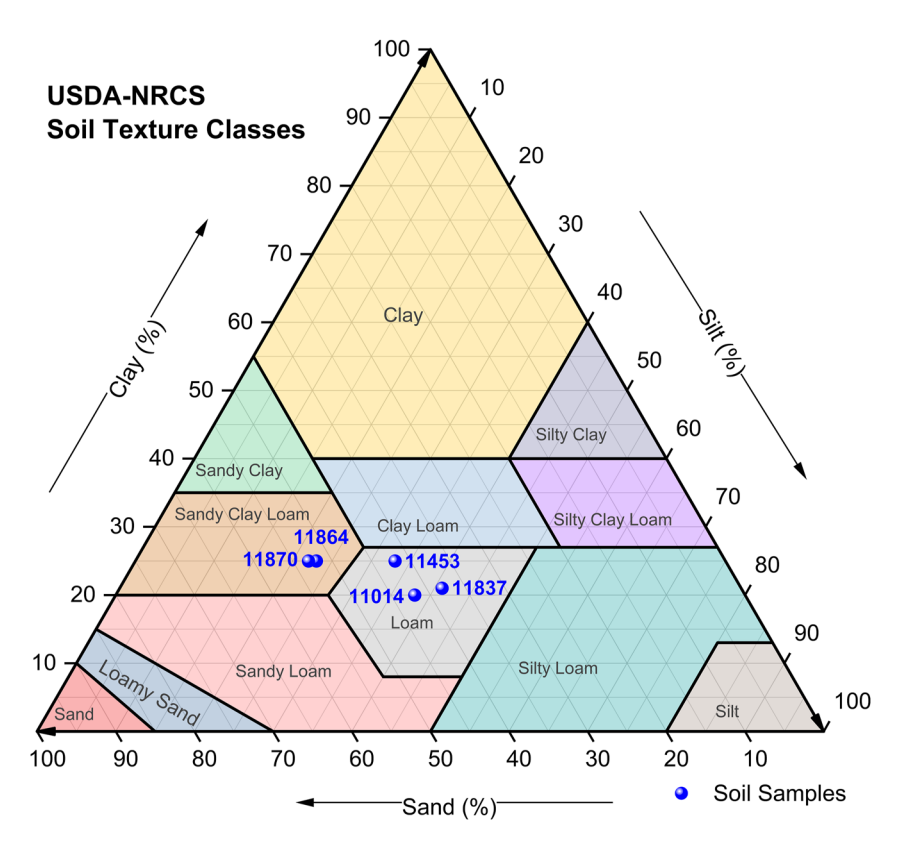
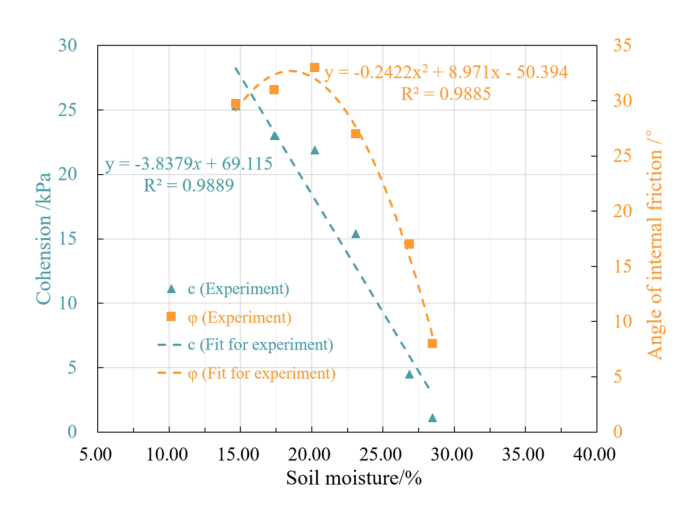


Figure 7. Soil texture diagram. There are five soil combinations of the ratio of clay, sand and silt in Jiangjia gully, as shown in Figure 5e. According to the U.S. Department of Agriculture classification system, there are two soil types: sandy clay loam and loam.

Abundant evidence shows that cohesion and internal friction angle change with the variation in water content (e.g., Matsushi & Matsukura, 2006; Mouazen et al., 2002). To improve the accuracy of the model, the influence of the water content on the cohesion and internal friction angle is considered. The relationships between cohesion and internal friction angle and water content are shown in Figure 8. The data come from the report of Hu et al. (2011). Figure 8 shows that the cohesion and internal friction angle in the Jiangjia gully exhibit a good correlation.



**Figure 8.** The relationships between the cohesive force  $c_{\text{soil}}$  and internal friction angle  $\varphi$  and water content (Hu et al., 2011).

## 4. Numerical Modeling Results and Analysis

The cohesion  $c_{\rm soil}$  (including the root strength), the internal friction angle  $\varphi$ , the soil bulk density  $\gamma_r$ , the maximum water content  $\theta_s=0.33$  and the residual water content  $\theta_r=0.03$  on which this article is based are available in Hu et al. (2011) and Chen et al. (2019). And the air-entry value  $h_b=0.902$  m is taken from the results of the experimental measurements by the IMHE. However, the soil moisture content  $\theta$  and soil type parameter  $\lambda$  usually need to be calibrated. Therefore, in this chapter, the hydrological process is calibrated. Then, the best fit result of the soil type parameter  $\lambda$  is simulated. Finally, the performance of the model is evaluated.

#### 4.1. Hydrological Model Calibration

It is necessary to note that proper model calibration is very important to reduce the error of the model output (e.g., Chen et al., 2020; Maharjan et al., 2013). The amount of observed runoff was used to calibrate the hydrological process. In this study, the free program swap-cup provided by the SWAT model official website was used to calibrate the hydrological runoff.

JIANG ET AL. 10 of 25

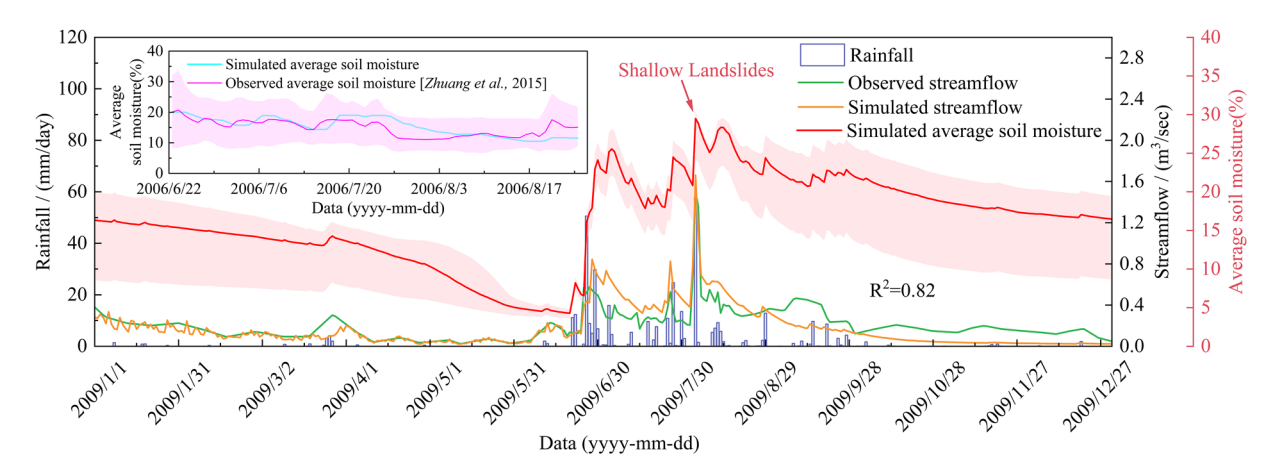


Figure 9. SWAT model runoff calibration results, correlation coefficient: NSE = 0.66,  $R^2 = 0.82$  (when NSE > 0.5 and  $R^2 > 0.6$ , the simulation results are usually perceived to be credible). Inset shows the comparison between simulated and measured soil moisture content for 22 June to 25 August 2006.

The calibrated model parameters are shown in Table 1, and the calibration results are shown in Figure 9. A comparison of the results shows that the calibration results exhibit satisfactory agreement with the observed results. The Nash-Sutcliffe *Efficiency* coefficient (NSE) is 0.66, and the Pearson Correlation coefficient ( $R^2$ ) is 0.86. Through the calibration of the hydrological process, the correctness of the soil moisture content is guaranteed to a certain extent. In addition, the calibrated parameters were used to invert the soil moisture content in the basin in 2006, as shown in the inset of Figure 9. This figure compares the simulated and observed soil moisture contents from 23 June to 25 August 2006. The results showed that the simulated and monitored soil moisture were basically consistent (Zhuang et al., 2015). In conclusion, the results of this simulation are reasonable.

Figure 9 also shows the changes in soil moisture content in 2009 as a numerical estimate. The average soil moisture reached a maximum of 29.5% on August 4. The only shallow landslides event recorded in 2009 also occurred on this day. In addition, there was almost no rain in the study area before June. The average moisture content of the soil was kept below 15.0% for a long time and was only approximately 4.3% at the lowest. However, the rainfall reached 51.2 mm/day (rainstorm level) on June 26, which was roughly equivalent to the rainfall on August 4 (57.7 mm/day). Although the soil water content increased sharply after heavy rain, reaching 2 times that before rain, the soil water content was still low due to long-term drought and the long-term lack of water in the soil. Therefore, under heavy rainfall, there were still no shallow landslides or debris flows in the study area. This also shows that it is difficult to accurately predict shallow landslides or debris flow events based on single-day rainfall and ignoring the influence of soil moisture content on soil mechanical properties (Table 2).

#### 4.2. Best Fit Scenario for Estimating Soil Type Parameters $\lambda$

Using the numerical modeling approach described in Section 2 and the parameters in Section 3, rainfall-induced shallow landslides were simulated. The duration of the simulation is set to 123 days, from 1 June 2009, to 1 October 2009. The simulation results are consistent with the observations, and shallow landslides occurred in the Jiangjia gully only on August 4. Therefore, we focus on the analysis of the simulation results on August 4, that is, the volume and spatial distribution of landslides.

Loam and sandy clay loam are the two main types of soils in the study area (in Section 3.3). Loam accounts for approximately 58.9% of the total area, and sandy clay loam accounts for approximately 41.1%. To fit the best soil type parameter  $\lambda$  in the study area, it is assumed that the parameter  $\lambda$  is constrained by the values of  $\lambda_L = 0.137$  to 0.355 for loam and  $\lambda_{SCL} = 0.125$  to 0.502 for sandy clay loam according to Rawls et al. (1982). The  $\lambda$  value of different permutations and combinations were simulated. The simulation scheme is shown in Table 3. The simulated and actual landslide areas within each sub-watershed were compared. The correlation coefficients between simulated and actual landslides under different soil types are calculated, as shown in Figure 10. When the soil type parameters are  $\lambda_L = 0.325$  and  $\lambda_{SCL} = 0.3$ , the simulation result are the closest to the inventory data, NSE = 0.8 and  $R^2 = 0.93$ . Obviously, the soil type has a great influence on the landslide volume, which was also reported in previous studies (Von Ruette et al., 2013). When the loam soil type parameter  $\lambda_L < 0.25$ , NSE <0, the simulation error is large.

JIANG ET AL. 11 of 25



Category	Parameter	Description	Min	Max.	Calibrated value
Runoff	CN2/C	SCS runoff curve number (%)	35	98	41.3
	OV-N	Manning's "n" value for land cover to estimate overland flow (%)	0.01	30	15.0
	CANMX	Maximum canopy storage (mm)	0	100	30.0
	SURLAG	Surface runoff lag time (hr)	0	24	12.0
Groundwater	ALPHA_BF	Baseflow alpha factor (shallow aquifer)	0	1.0	0.1
	GWQMN	Threshold depth of water in the shallow aquifer required for return flow to occur (mm)	0	1000	450
	REVAPMN	Minimum depth of water in shallow aquifer for re-evaporation to occur	0	200	180
	GW_DELAY	Groundwater delay (days)	0	450	72.0
	GW_REVAP	Groundwater "revap" coefficient	0.02	0.2	0.07
	SOL_AWC()	Available water capacity of the soil layer (mm/h)	0	1	0.7
	SOL_K()/ Ksat	Saturated hydraulic conductivity (mm/h)	0	900	108.3
Soil/Plant	EPCO	Plant uptake compensation factor	0	1	0.9
	ESCO/ Es"	Soil evaporation compensation factor	0	1	0.7
Reach	CH_K2	Effective hydraulic conductivity in main stream alluvium (mm/hr)	0.01	500	150.0
	CH_N2	Manning's "n" value for the main stream	0	0.3	0.09

#### 4.3. Comparison of the Shallow Landslides List of Observed and Simulated

To verify the predictive performance of this model at the landslide scale, the density-based spatial clustering and other algorithms were employed to cluster adjacent damaged soil columns together to generate landslide polygons, which enables one to eliminate outliers from the data set. The area and volume of the shallow landslides were calculated after clustering, and these results were compared with the observed shallow landslides (the data are from the Jiangjia gully debris flow observation station, including the elevation difference of the DEM before and after the landslide), as shown in Figure 11. Figure 12 shows the cumulative distribution function (CDF) of the simulated single landslide area and the measured landslide scar area from inventory data. The results show that the simulated soil depths are in good agreement with measured landslide thickness. In addition, the entire watershed was classified into 16 sub-watersheds depending on watershed topography, and the depth, area, and volume of the shallow landslide soil column in each sub-basin were calculated (Figures 13 and 14). The results (in Figure 13) show that both the landslide inventory and simulation reproduce the power law relationship.

A comparison of the simulated landslide depth with the observed landslide depth of each sub-watershed is shown in Figure 13. The results show that the simulated landslide soil depth is 0.72-1.77 m, whereas the observed landslide soil depth is 0.55-1.65 m. The average simulated and observed landslide soil depths are 0.764 and 0.729, respectively. The simulated landslide depths are slightly deeper than the actual landslide depths, which could be related to the overestimation of the wetting front depth. In this model, only the one-dimensional vertical infiltration considered, not the lateral flow of groundwater. The benefit of this is simplification is a reduction in computational costs, the downside being that the depth of the wet front may be overestimated, resulting in a deeper predicted landslide depth. Figure 14 shows a comparison of landslide area and volume. The area is the area of the clustered landslides, and the volume is the product of the average depth of the failed soil column and the area of the clustered landslides. The results show that the simulation is satisfactory. The correlation coefficients of the simulated and actual landslide volumes and areas are NSE = 0.81 and 0.80 and  $R^2 = 0.94$  and 0.93, respectively.

Table 3Parameter  $\lambda$  Setting Scheme of the Soil Spatial VariabilitySoil typeSoil type parameter  $\lambda$ Loam  $(\lambda_L)$ 0.2, 0.225, 0.25, 0.275, 0.3, 0.325, 0.35Sand clay loam  $(\lambda_{SCL})$ 0.2, 0.3, 0.4, 0.5

#### 4.4. Validation of the Numerical Results

To further evaluate the performance of the model, the shallow landslide was simulated with rainfall during the two-year period 1999–2000, using the parameters calibrated above. According to the observation data, landslide events occurred on a total of 16 days in 1999–2000. The simulation results show that disaster events occurred on a total of 15 days in 1999–2000. The

JIANG ET AL. 12 of 25

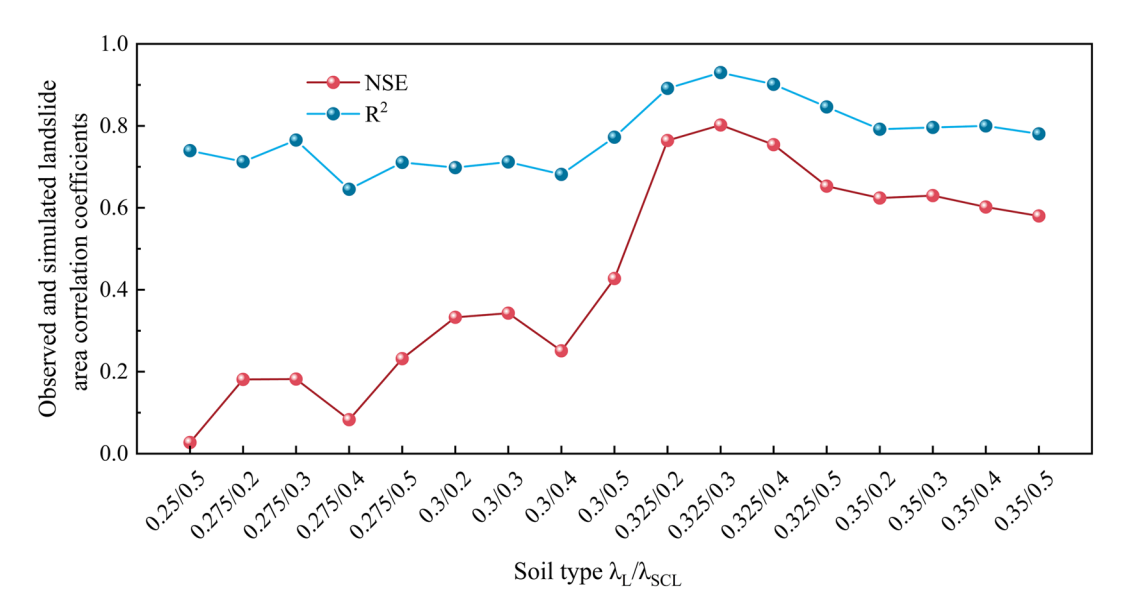


Figure 10. Numerical results of the landslide area correlation coefficients. The case of NSE <0 is not shown in the picture.

occurrence times of 13 debris flows are consistent with the observation data, and the accuracy of the occurrence time of debris flow disaster prediction is 81.25%. Figure 15 shows that the simulation results misreport two landslide events on 23 July 1999, and 3 September 1999, and miss three landslide events on 5 August 1999, 19 June 2000, and 6 July 2000. Figure 16 shows the relationship between the observed and the predicted volumes. The error in the volume of the shallow landslide volume predicted by the model is in the range of -40% to +50%.

Although the simulation results of the model still deviate from the observation data and may miss small-scale debris flow events, this is unavoidable and is related to many factors (e.g., soil parameters, climate, and rainfall). The deviation of rainfall data is an important source of forecast error. The Jiangjia gully watershed has a large area, and there are significant differences in local rainfall in the region. In this study, the average rainfall collected by three rainfall devices distributed at different locations in the watershed was used (in Figure 11). The error formed using the average rainfall may be an important reason for the deviation in the simulation prediction results. In

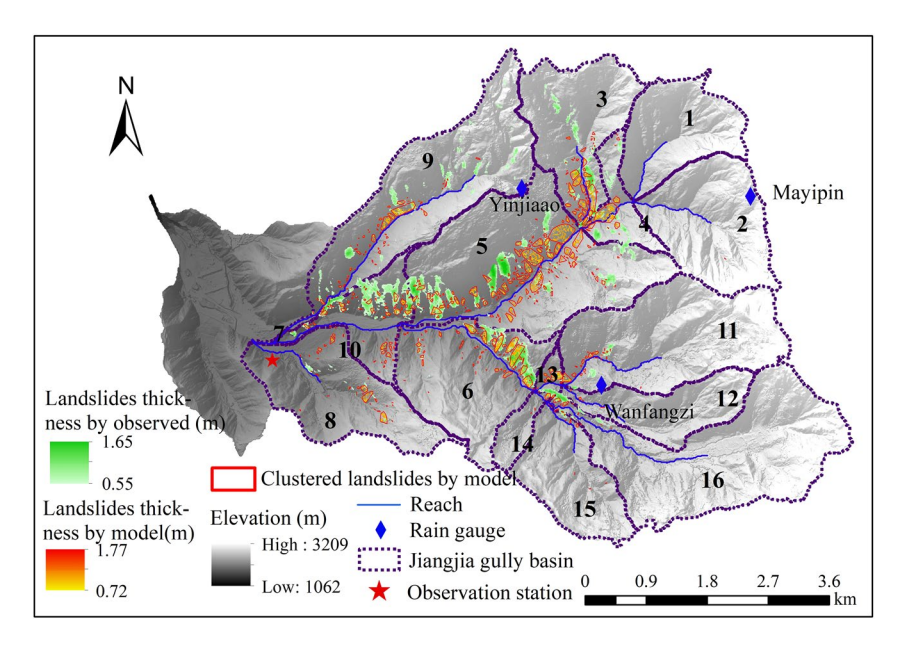
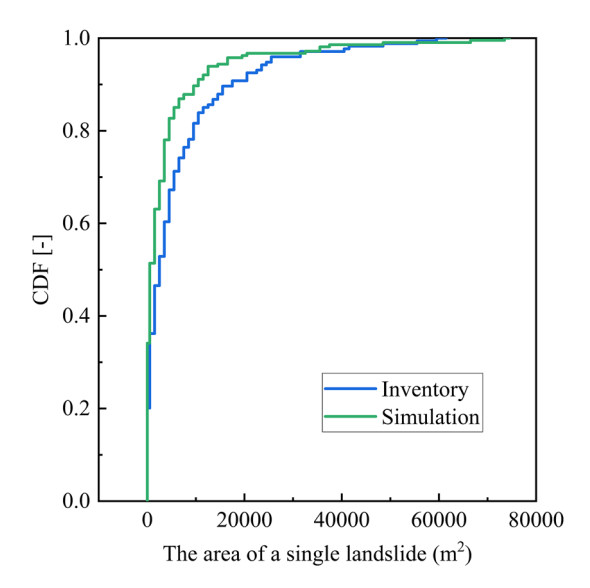


Figure 11. Comparison of model and observed landslide depth and distribution. The black numbers are sub-basin numbers 1-16.

JIANG ET AL. 13 of 25



**Figure 12.** Cumulative distribution of the simulated landslide area and the measured landslide scar area from inventory data.

addition, according to the historical observation data, the volumes of these 3 disasters, which occurred on 5 August 1999, 19 June 2000, and 6 July 2000, were relatively small, with shallow landslide volumes of  $0.8 \times 10^4$  m<sup>3</sup>,  $7.24 \times 10^4$  m<sup>3</sup>, and  $6.3 \times 10^4$  m<sup>3</sup>, respectively. Due to the large watershed area of Jiangjia gully, there are still deposits left over from shallow landslides in the channel. Not every debris flow event triggers a new shallow landslide, especially small-scale debris flow events. This may cause the model to fail to accurately predict this type of event. Because this is a catchment-scale model, this model does not aim to predict the volume of shallow landslides very accurately but aims to be consistent regarding the order of magnitude. Therefore, the simulation results of the model are satisfactory.

Finally, we would like to emphasize that although the established numerical model simulates shallow landslides caused by rainfall well, its limitations and particularities must be explicitly understood (Subramanian et al., 2020). First, to obtain better prediction results, complete and accurate soil physical parameters and rainfall data are needed. Second, in our model, soil pillars may still be damaged along the soil-rock interface, so soil depth is still important. Third, the SWAT model is semi-empirical but proves to be effective for the purpose of this study. In addition, in the process of calculating soil instability in each rainfall time step, 1 day's rainfall is considered the application condition. The progressive instability process of the landslide in the current

state is calculated until the soil column reaches static equilibrium, and then start the next rainfall time step starts. The purpose is to achieve long-term forecasting, over months or even a year. Therefore, the time scale of rainfall is daily in this simulation (e.g., Godt et al., 2012; Kuriakose et al., 2010; Subramanian et al., 2020). However, the destruction of shallow landslides usually takes a short time and may even occur within a few seconds. Therefore, to improve the prediction efficiency and accuracy, it is also necessary to establish a prediction model with a shorter time scale (e.g., hour-scale, minute-scale or second scale) and to couple it with this model.

#### 5. Discussion

In this section, the sensitivity of analytical models to rainfall and root strength is discussed by establishing artificial rainfall patterns and root strengths, and the error of the model is analyzed.

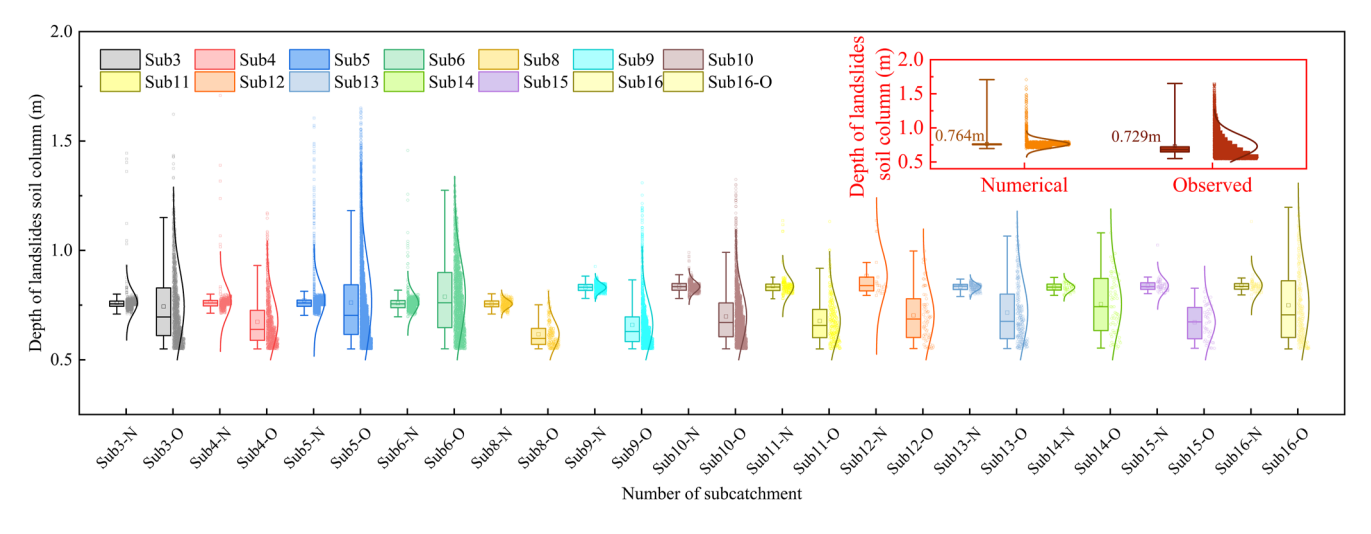


Figure 13. Comparison of the simulated and observed landslide depths; each point represents a soil column. Sub3-N and Sub3-O represent the numerical and observed soil column failure depths in sub-watershed 3, respectively. The inset is a boxplot of the depth of the landslide soil column. The average failure depth of the simulated and observed soil column is 0.764 and 0.729, respectively.

JIANG ET AL. 14 of 25

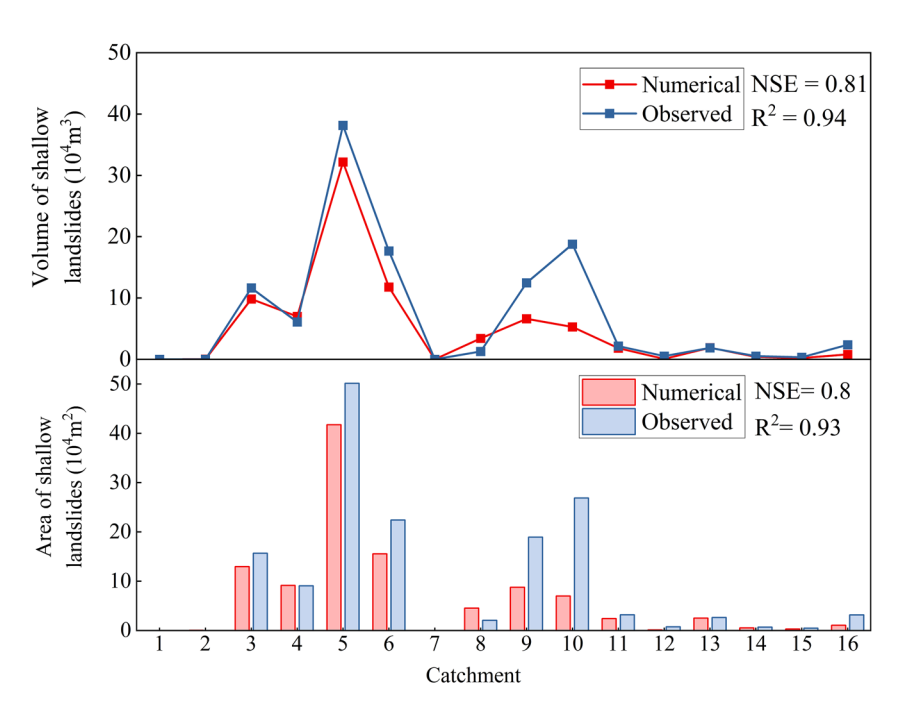


Figure 14. Comparison of the simulated and observed landslide areas and volumes. The results show that the simulation results are satisfactory, the landslide volume correlation coefficients are NSE = 0.81 and  $R^2$  = 0.94; the landslide area correlation coefficients are NSE = 0.8 and  $R^2$  = 0.93.

#### 5.1. The Effect of Same-Day Rainfall Intensity on Landslides

Three landslide events were selected randomly, 16 July 1999, 24 June 2014, and 4 August 2009, to simulate the effect of different rainfall intensities on the same day on the landslides volume. The initial water contents of the three landslides events are 0.126, 0.105, and 0.097, respectively. Figure 17 shows the effect of different same-day rainfall events on landslide volume. The results showed that the landslide volume increased with the same-day rainfall. The initial soil moisture content significantly affects the volume of the landslides. The higher the initial soil moisture content is the larger volume of the landslide. It can be expected that under dry conditions (unsaturated), the shear strength of the soil mass is higher, reducing the possibility of landslides.

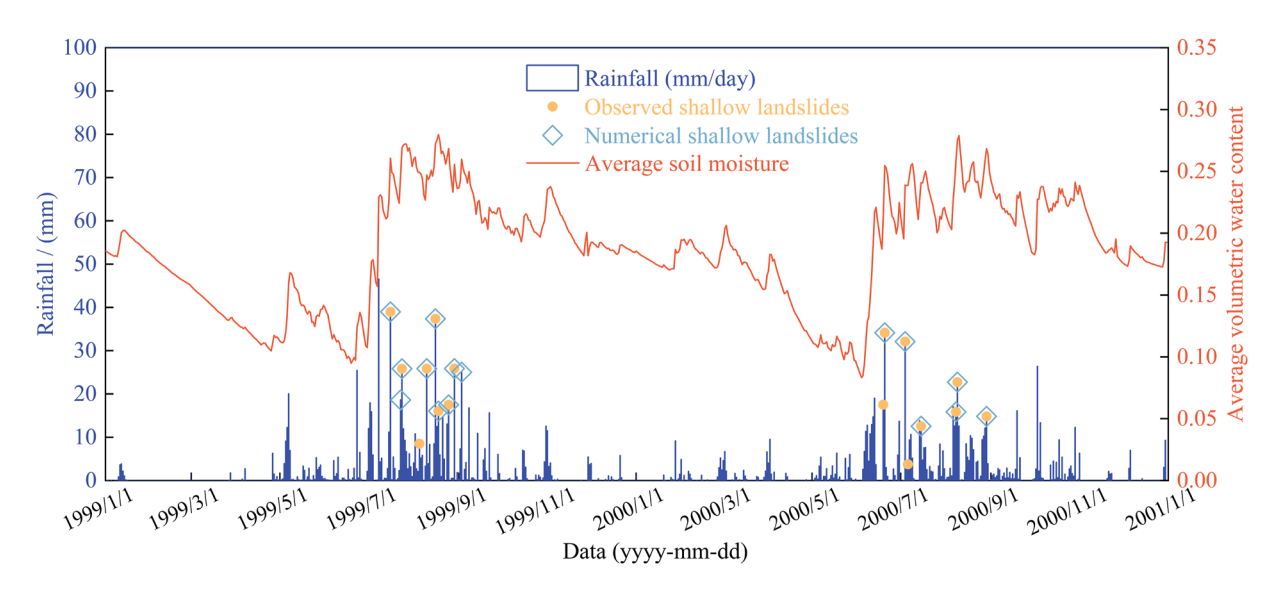
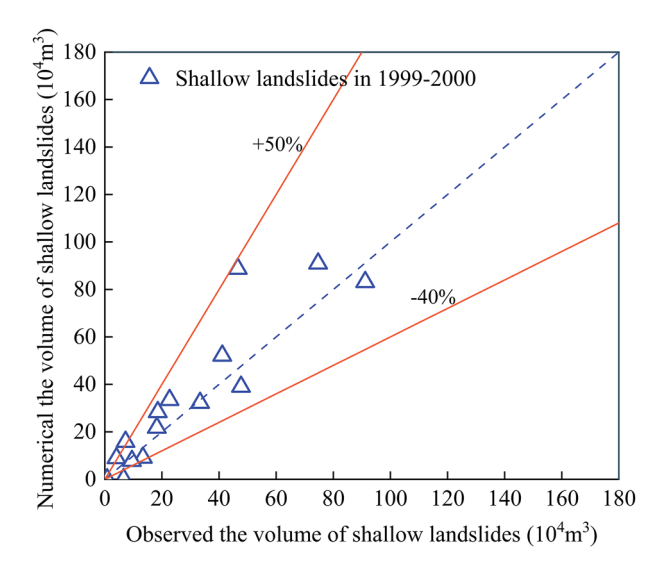


Figure 15. Rainfall and average soil moisture content in the 2 years of 1999–2000 (daily). The model predicted and observed shallow landslides in the watershed occurred on the days marked by brown diamonds and magenta circles, respectively.

JIANG ET AL. 15 of 25



**Figure 16.** Relationship between the observed and simulated landslide volume from 1999 to 2000. Each point represents a landslide event, with a total of 15 landslide events.

#### 5.2. The Effect of Antecedent Rainfall on Landslides

While the rainfall infiltration effects on landslides or shallow landslides have been studied extensively, no consensus has emerged about the antecedent rainfall on shallow landslides (e.g., Aleotti, 2004; Brand, 1984, 1992; Jemec & Komac, 2013; Ma et al., 2014; Rahardjo et al., 2007; Rahimi et al., 2011). Obviously, antecedent rainfall has an important effect on shallow landslides in the Jiangjia gully, but different antecedent rainfall values may have varying degrees of impact (Jonathan et al., 2006). This difference may be related to the effect of antecedent rainfall changes on the soil moisture content. It has been shown that as the initial soil moisture content before rainfall increases, matrix suction decreases, and thus the volume of landslides increases. To further explore the effect of antecedent rainfall on shallow landslides, first, the average soil moisture content was simulated under different previous rainfall patterns (in Figure 18). Taking the landslides event on 16 July 1999, as an example, 8 precipitation patterns were designed for a total of 20 days

from 25 June 1999, to 15 July 1999, numbered No. 1 to No. 8. The total antecedent rainfall TP<sub>20</sub> (TP<sub>n</sub> =  $\sum_{i=1}^{i=n} P_i$ ) of these 8 rainfall patterns is 120 mm, and the weight of the antecedent rainfall AP<sub>20</sub> gradually increases with the numbers No. 1–No. 8. The formula of antecedent rainfall AP<sub>20</sub> was as follows (Woldemeskel & Sharma, 2016):

$$AP_n = \sum_{i=1}^{n} P_i K^i \tag{12}$$

 $P_i$  is the rainfall on the i day before the landslides event, K is the decay factors (ranging from 0.4 to 1.0, Take 0.8 in the study area), and n is the total number of days (Take 20 in this study).

Figure 18 shows the relationship between the weight of the antecedent rainfall and the initial soil moisture content before the rainfall on 16 July 1999. This show that with increasing weighted antecedent rainfall  $AP_{20}$ , the initial soil moisture before rainfall first increases and then decreases. Comparing the eight rainfall patterns, it can be seen that the larger the pre-weighted rainfall value, the more concentrated the rainfall is in the first few days of the landslides. Taking No. 8 as an example, the rainfall in the two days before the disaster accounted for 81% of the accumulated

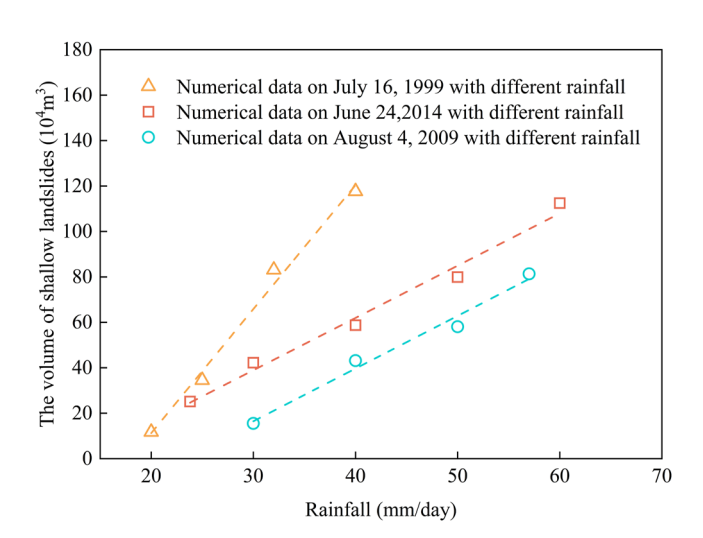


**Figure 17.** The relationship between different same-day rainfall intensities and landslides volumes. The brown, blue, and red dashed lines are the simulated fit lines of 16 July 1999, 24 June 2014, and 4 August 2009. The initial soil moistures are  $\theta_0 = 0.126$ ,  $\theta_0 = 0.105$ , and  $\theta_0 = 0.097$ , respectively.

rainfall in the first 20 days, which led to a very low soil moisture content before July 13, even though rainfall occurred on the 14th and 15th. Even with higher intensity rainfall, the soil moisture content still did not reach a high value. The inset of Figure 18 shows the relationship between peak rainfall and cumulative runoff (26 June–16 July 1999). The results show that the higher the peak rainfall, the higher the total cumulative runoff. The reasons is that the infiltration time is short, and the high-intensity rainfall are exceeding soil infiltration capacity and convert more water into surface runoff, which leads to a lower soil infiltration. A similar result was obtained in a study by Fan et al. (2020). Therefore, with increasing weighted previous rainfall, the initial soil moisture first increased and then decreased.

Figure 19 also shows the relationship between the pre-weighted rainfall and the volume of the landslides. As the pre-weighted precipitation increases, the volume of the landslides first increases and then decreases. The reason for this is that the landslide volume increases with the initial soil moisture content before rainfall. In summary, the pre-weighted rainfall can be used for the quantification of different pre-rainfall models, but the landslide volume does not increase with increasing pre-weighted rainfall but first increases to the peak and then decreases slightly. The above results confirm that early rainfall mainly controls the soil water content, affecting the volume of the

JIANG ET AL. 16 of 25

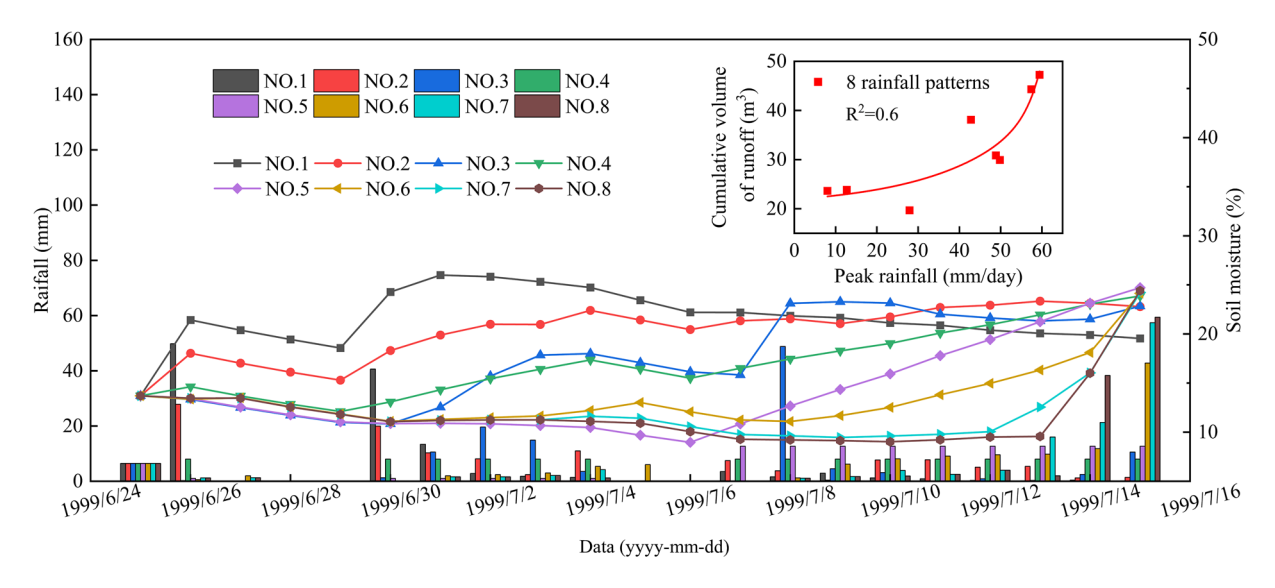
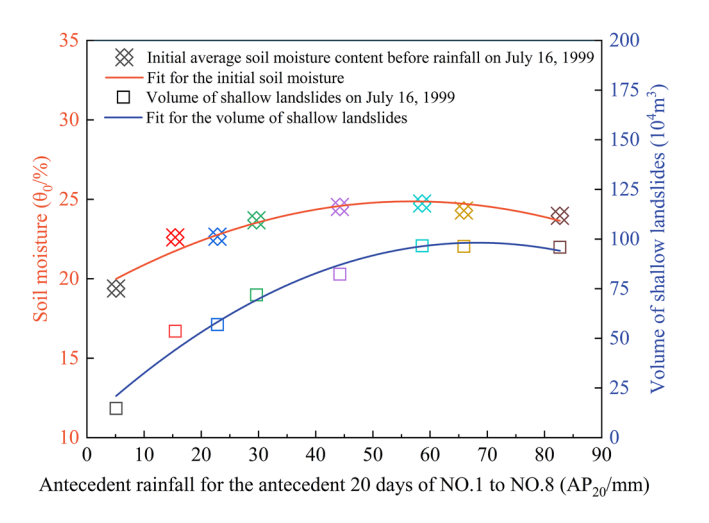


Figure 18. Average soil moisture content curve and rainfall intensity with 8 antecedent rainfall patterns. The inset shows the relationship between peak rainfall and cumulative runoff (26 June–16 July 1999) for the 8 antecedent rainfall patterns. Each point represents a rainfall pattern, with a total of 8 antecedent rainfall patterns.

landslides. If the effect of antecedent rainfall on soil moisture content is not considered, it may cause very large prediction deviations.

Although the rainfall threshold can reflect the relationship between rainfall and the occurrence of landslides or debris flows to a certain extent, this method ignores the changes in the soil mechanical properties from the effect of moisture content and often has large errors. The instability of the slope is often controlled by the soil moisture content. Figure 20 shows the relationship between the weighted value of previous rainfall and the sum of rainfall on the same day and the soil moisture content after rainfall. With increasing rainfall, both the average soil moisture content and the landslide volume show increasing trends. When the average soil moisture content is greater than 24.03%, there is a possibility of shallow landslides in the watershed, otherwise, there are no landslides.



**Figure 19.** The red line is the relationship between the antecedent weighted rainfall value and the initial soil moisture content. The blue line is the relationship between the antecedent weighted rainfall and landslide volume.

## 5.3. The Effect of the Root Strength on Landslides

The root system of vegetation is very complex and difficult to quantify. Different quantification methods may lead to different root strengthening values (Schmidt et al., 2001). The experimental measurement of the root strength of individual roots was used to quantify the mechanical reinforcement of roots (in Section 3.2). However, in a soil column grid, the number and spacing of plants may cause differences in the mechanical reinforcement of vegetation roots. This method may overestimate the mechanical reinforcement effect of vegetation roots (e.g., Schwarz et al., 2010; Sidle & Ochiai, 2006). However, there are no large-scale shallow landslides in the vegetation area of the Jiangjia gully watershed (Tian et al., 2021). Overestimating the mechanical strength of the root system does not have a very large impact on the prediction results. However, many actual cases in other regions show that even with the mechanical reinforcement of the root system of vegetation, larger-scale shallow landslides may still be triggered (e.g., Netto et al., 2011; Yang et al., 2020). Therefore, it is necessary to explain the influence of root mechanical reinforcement strength on shallow landslides. We multiply the experimental measurement value by a coefficient  $\eta$  to simulate different root mechanical reinforcement strengths. The effect of the root mechanical strength on the landslide damage volume is shown in Figure 21. As the mechanical strength of the root system decreases, the volume of the landslides gradually increases, indicating that mechanical root reinforcement

JIANG ET AL. 17 of 25

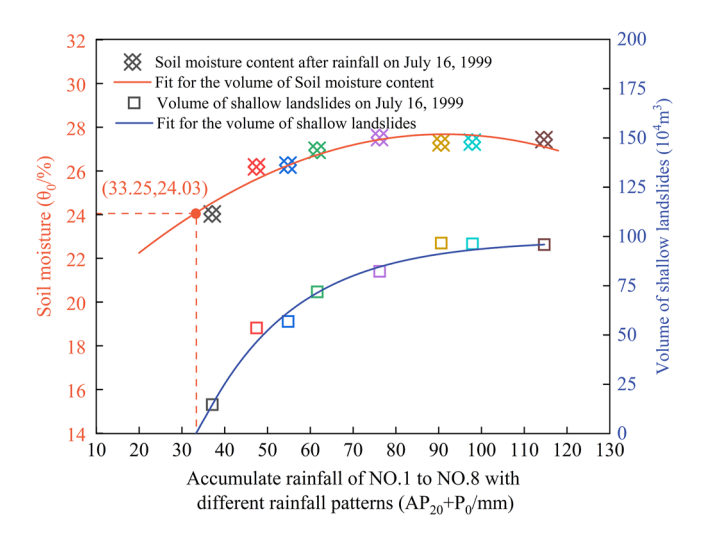


**Figure 20.** The red line is the relationship between  $AP_{20} + P_0$  (the sum of antecedent weighted and same-day rainfall) and the soil moisture content. The blue line is the relationship between  $AP_{20} + P_0$  and the landslide volume. The red triangle points indicate that shallow landslides may occur in the watershed when the average soil moisture content is greater than 24.03%.

can effectively reduce shallow landslides. In addition, when the root strength reduction coefficient is small, the volume increase ratio of shallow landslides gradually decreases with increasing rainfall. This shows that with increasing rainfall, the influence of vegetation on the volume of shallow landslides decreases. Therefore, in extreme weather conditions, mechanical reinforcement of plant roots may be ineffective and even promotes the occurrence of shallow landslides (Yang et al., 2020).

The roots, animal carcasses and decaying plants usually form numerous pore channels, which allow the rainfall to quickly transfer to the potential slip plane, possibly passing through the wetting front to reach deeper potential sliding surfaces. This could lead to larger shallow landslides. The root tip is usually the first place where water reaches and pools, resulting in an increase in local soil moisture content and local pore water pressure, thereby reducing soil structural strength and increasing soil sliding force. When the unfavorable factors of vegetation root diversion offset the mechanical reinforcement of the slope by the vegetation, the vegetation is not conducive to the stability of the slope.

## 6. Summary and Conclusions

In this paper, the SWAT model and the D-LHT model are combined to develop a catchment-scale, day-scale numerical model to analyze soil slope

instabilities induced by rainfall. The SWAT model considers hydrological processes such as vegetation evapotranspiration and canopy interception, which improves the accuracy of the coupled model.

Additionally, the model established in this paper does not limit the sliding surface to only the bedrock surface but calculates the depth of the wetting front through rainfall infiltration. Additionally, the iterative calculation method was used to search the most dangerous sliding surface in the soil profile. It also expands the scope of application of the coupling model. Some process-based insights from this study are summarized as follows:

- 1. According to forecasted daily rainfall data, the proposed model can be used to predict the date, scale, and spatial distribution of shallow landslides well in advance.
- 2. The sensitivity analysis results show that the model is highly sensitive to the soil type, soil moisture content, slope, and internal friction angle.
- 3. Single-day rainfall is an important external factor affecting soil stability but is not the only decisive factor. When shallow landslides or debris flow events are predicted, the synergistic effects of various factors such as

changes in soil water content, soil mechanical properties, and internal friction angles should be considered.

In general, the numerical model adopted in this paper can not only predict the date, spatial distribution and volume of landslides but also provide a reference for deducing the occurrence time, scale, and spatial distribution of most landslides in small basins with sparse data. It provides a possible new method for real-time shallow landslides instability prediction and warning systems. We intend to use the model for more case studies in the future and expect our model to be incorporated into an early warning system to analyze and predict multiple occurrences of landslides simultaneously and to issue alert messages.

Additionally, only one-dimensional vertical infiltration of water was considered in this model, and the lateral flow of groundwater was neglected. This approximation could improve the computational speed of the model but could also bias the physical understanding of shallow landslide triggering. Further effort is required to advance the physical understanding of shallow landslide triggering at the watershed scale in a fully three-dimensional, time-dependent context.

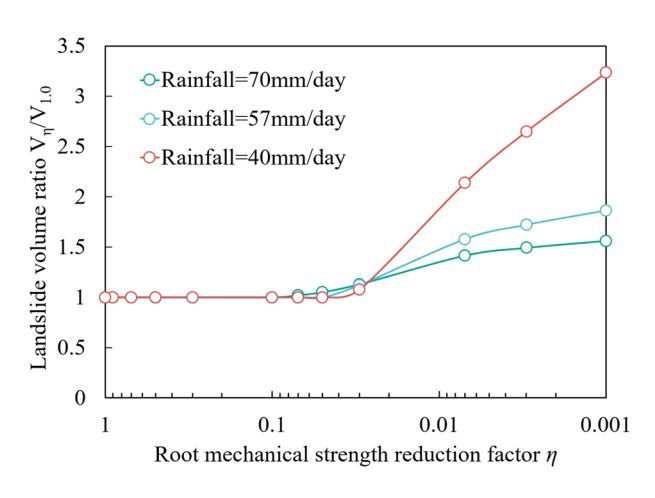


**Figure 21.** The influence of root mechanical strength on landslides volume, where  $V_{\eta}$  is the landslide volume and  $V_{1.0}$  is the landslide volume when the reduction factor  $\eta = 1.0$ .

JIANG ET AL. 18 of 25



## Appendix A: The SWAT Hydrological Model

On the basis of several sub-watersheds dividing the watershed, the SWAT model performs overlay analysis according to land use, topography, and soil data and generates a smaller modeling unit called the Hydrological Response Unit (HRU) according to their unique combination relationship. Therefore, watersheds are heterogeneous, while HRUs are homogeneous. Each HRU is the minimum calculation unit of the SWAT model, which calculates the overall water balance of the HRU by calculating processes such as precipitation, interception, filling, runoff, evaporation, infiltration (and regression flow). To avoid reducing the calculation efficiency of the model due to too many HRUs, identical HRUs within the same sub-basin are merged. The hydrological response unit is composed of multiple quadrilateral grids. After the calculation of the hydrological process, the basic data on the original quadrilateral grid is interpolated to the hexagonal grid by the inverse distance weighting method. Then, the hexagonal grid is used to calculate the instability failure of the soil (Von Ruette et al., 2013). For ease of presentation, after the simulation, the hexagonal grid is interpolated to a quadrilateral grid in the same way.

#### A1. Runoff

In this model, surface runoff is simulated by the Soil Conservation Service (SCS) model, which requires fewer parameters and is not limited to existing measured data. This method can accurately simulate the runoff generated by the underlying surface of various land use types and soil types. The formula for surface runoff is as follows:

$$Q_{\text{surf}} = \frac{(R_d - I_a)^2}{R_d - I_a + S}$$
 (A1)

where  $Q_{\text{surf}}$  is the surface runoff (mm),  $R_d$  is the rainfall (mm),  $I_a$  represents the infiltration, evapotranspiration and interception-induced rainfall losses (mm), S is the maximum possible retention (mm), and  $S = 25.4 \left( \frac{1000}{C} - 10 \right)$ , where C is a parameter that reflects the pre-water condition of the soil, which is obtained by calibration, and is denoted by CN2 in Table 2. The condition for generating runoff is that the daily precipitation is greater than the initial rainfall loss.

#### A2. Evapotranspiration

The calculation of evapotranspiration mainly includes plant and soil evapotranspiration. The calculation formula of plant evapotranspiration is as follows:

$$\begin{cases} E_t = \frac{\text{LAI}}{3.0} * E'_0 & 0 \le \text{LAI} \le 3.0 \\ E_t = E'_0 & 3.0 \le \text{LAI} \end{cases}$$
 (A2)

where  $E_t$  is the maximum plant transpiration (mm),  $E'_0$  is the potential evapotranspiration (mm), and LAI is the leaf area index (mm<sup>2</sup>/mm<sup>2</sup>).

The calculation formula of soil moisture evapotranspiration is as follows:

$$E_{\text{soil},z} = E_s'' \frac{z}{z + \exp(2.347 - 0.00713 * z)} \tag{A3}$$

where  $E_{\text{soil},z}$  is the soil moisture evapotranspiration (mm),  $E_s''$  is the potential soil evaporation (mm), and z is the soil depth (mm).

### A3. Soil Water

The calculation formula of the water volume lost to seepage is as follows:

$$w_{\text{seep}} = 0.024 \left( \frac{2 * SW_{\text{ly,excess}} * K_{\text{sat}} * \text{SLP}}{\varphi_d * L_{\text{hill}}} \right)$$
(A4)

JIANG ET AL. 19 of 25



where SW<sub>ly,excess</sub> is the discharge water volume in the soil-saturated layer (mm),  $K_{\text{sat}}$  is the saturated hydraulic conductivity of the soil (mm/h), SLP is the average slope of a HRU (mm/mm),  $\varphi_d$  is the porosity (mm/mm), and  $L_{\text{hill}}$  is the slope length (m).

#### A4. Ground Water

Ground water exists in the baseflow forms and is a stable recharge source of surface runoff. The calculation formulae are as follows.

$$Q_{\text{gw},i} = Q_{\text{gw},i-1} \exp(-\alpha_{\text{gw}} * \triangle t) + W_{r,i} \left[ 1 - \exp(-\alpha_{\text{gw}} * \triangle t) \right]$$
(A5)

$$W_{r,i} = \left[1 - \exp\left[-\frac{1}{\delta_{\text{gw}}}\right]\right] * w_{\text{seep}} + \exp\left(-\frac{1}{\delta_{\text{gw}}}\right) * W_{r,i-1}$$
(A6)

Where  $\alpha_{\rm gw}$  is the dissipation factor of ground water,  $W_{r,i}$  is the water input into the groundwater reservoir in step i (mm),  $Q_{{\rm gw},i}$  is the groundwater flowing into the river channel in step i (mm), and  $\delta_{\rm gw}$  is the lag time for water input into the groundwater reservoir (h).

## Appendix B: Determining the Direction of the Soil Column Instability

We number the six surrounding soil pillars No. 0 to No. 5 (k = 0, 1, 2, 3, 4, 5) and establish the positional relationship between the soil pillars. The barycentric coordinates of the central soil column i, j is expressed as  $(x_{i,j}, y_{i,j}, z_{i,j})$ . The horizontal distance between centers of hexagonal cells is  $L_g$ . The barycentric coordinates of the adjacent soil columns are expressed as:

$$\begin{cases} x_k = \frac{\sqrt{3}}{3} L_g \cos\left(\frac{k}{3}\pi\right) + x_{i,j}, \\ y_k = \frac{\sqrt{3}}{3} L_g \cos\left(\frac{k}{3}\pi\right) + y_{i,j}, \\ z_0 = z_6 = z_{i,j+1}, z_1 = z_{i-1,j}, z_2 = z_{i-1,j-1}, \\ z_3 = z_{i,j-1}, z_4 = z_{i+1,j-1}, z_5 = z_{i+1,j} \end{cases}$$
(B1)

The vector coordinates from the center of gravity of adjacent soil columns to the center of gravity of the central soil column  $(x'_k, y'_k, z'_k)$  are expressed as:

$$\begin{cases} x'_k = \frac{\sqrt{3}}{3} L_g \cos\left(\frac{k}{3}\pi\right) \\ y'_k = \frac{\sqrt{3}}{3} L_g \cos\left(\frac{k}{3}\pi\right) \\ z'_k = z_k - z_{i,j} \end{cases}$$
(B2)

The sum vector coordinates of adjacent soil columns  $\left(x_{k,k+1}',y_{k,k+1}',z_{k,k+1}'\right)$  are expressed as:

$$\begin{cases} x'_{k,k+1} = \frac{\sqrt{3}}{3} L_g \cos\left(\frac{k}{3}\pi\right) + \frac{\sqrt{3}}{3} L_g \cos\left(\frac{k}{3}\pi\right) \\ y'_{k,k+1} = \frac{\sqrt{3}}{3} L_g \cos\left(\frac{k}{3}\pi\right) + \frac{\sqrt{3}}{3} L_g \cos\left(\frac{k}{3}\pi\right) \\ z'_{k,k+1} = z_k + z_{k+1} \end{cases}$$
(B3)

The projection vector of the center of gravity vector in the xy plane is  $D_{k,k+1}$  (k = 0, 1, 2, 3, 4, 5). The projection vector of the movement direction vector of the central soil column on the two-dimensional plane is  $(x_{i,j}'', y_{i,j}'')$ .

According to the principle of least action, the sum vector with the lowest center of gravity  $\min(z'_{k,k+1})(k=0,1,2,3,4,5)$  is taken as the direction vector of soil column movement. The projection vector of

JIANG ET AL. 20 of 25



the movement direction of the central soil column on the two-dimensional plane is expressed as  $(x''_{i,j}, y''_{i,j})$ , where  $x''_{i,j} = x'_{k,k+1}$  and  $y''_{i,j} = y'_{k,k+1}$ . The projection vector of the movement direction of the surrounding soil column on the two-dimensional plane is expressed as  $(x''_k, y''_k)$ .

The formula for calculating the angle between adjacent soil columns is as follows:

$$\theta_k = \arccos \frac{x_{i,j}'' * x_k'' + y_{i,j}'' * y_k''}{\sqrt{x_{i,j}'^2 + y_{i,j}''^2} \sqrt{x_k''^2 + y_k''^2}}$$
(B4)

When the angle between the movement direction vectors of adjacent soil columns is an acute angle, then the force between the soil columns is compressive; when the angle between the movement direction vectors of the adjacent soil columns is an obtuse angle, then the force between the soil columns is tensile.

$$\begin{cases}
\text{If } \theta_k < \frac{\pi}{2} \text{ then } \tau'_{T,k} = -\tau_{T,k} \\
\text{If } \theta_k = \frac{\pi}{2} \text{ then } \tau'_{T,k} = 0 \\
\text{If } \theta_k > \frac{\pi}{2} \text{ then } \tau'_{T,k} = \tau_{T,k}
\end{cases}$$
(B5)

where  $\tau_{T,k}$  represents the force exerted on the central soil column by a surrounding soil column that is unstable.  $\tau'_{T,k}$  represents a force exerted on the central soil column by the surrounding soil column and is used to calculate the sliding force.

#### **Notation**

 $N_I$ 

**NSE** 

$lpha_{ m gw}$	the dissipation factor of groundwater.
$A_H$	the area of a soil column with a hexagonal cross-section, m <sup>2</sup> .
$A_i$	the intersection area between two adjacent columns, m <sup>2</sup> .
$A_{ m RAR}$	the ratio of the root area and the area with rooted soil.
$c_{ m soil}$	the soil cohesion, $kg/(m s^2)$ .
$\delta_{ m gw}$	the lag time for water input the reservoir of ground water, h.
$E_a$	the water volume lost via evapotranspiration in step $i$ , m.
$E_0' \ {E_s}''$	the potential evapotranspiration, m.
$E_s^{\prime\prime}$	the potential soil evaporation, m.
$E_{\mathrm{soil},z}$	the soil moisture evapotranspiration, m.
$E_t$	the maximum plant transpiration, m.
FOS	the factor of safety.
g	the acceleration due to gravity, ms <sup>-2</sup> .
h	the capillary pressure head, m.
$h_b$	the air-entry value, m.
$h_s$	the height of the free water table in the soil column, m.
$H_d$	the distance from the sliding interface to the ground surface, m.
$H_{ m pond}$	the depth of runoff, m.
I	the total infiltration of water, m.
$I_a$	the infiltration evapotranspiration and interception-induced rainfall losses, m.
K	a dimensionless correction parameter.
$K_{\mathrm{sat}}$	the saturated hydraulic conductivity of the soil, $m h^{-1}$ .
λ	the pore size distribution parameter.
LAI	the leaf area index
$L_{ m hill}$	the slope length, m.
Lg	Lg, m.
M	the total mass of a soil column, kg.

JIANG ET AL. 21 of 25

the compressive load acting on the column.

the Nash-Sutcliffe efficiency coefficient.



Ψ	the porosity.
$oldsymbol{arphi}_d$	the porosity.
$Q_{ m gw}$	the total underground water in step $i$ , m.
$Q_{\mathrm{gw},i}$	the groundwater of flowing into the river channel in step $i$ , m.
$oldsymbol{Q}_{ ext{surf}}$	the total surface runoff in step $i$ , m.
R	the total precipitation in step $i$ , m.
$R_d$	the rainfall, m.
$SW_t$	the end water content of a time step in the SWAT model.
$sw_0$	the soil moisture content at the previous time step in the SWAT model.
$\boldsymbol{S}$	the maximum possible retention, m.
$SW_{ly,excess}$	the discharge water volume in the soil-saturated layer, m.
SLP	the average slope.
$S_f$	the slope, °.
Θ	the effective water saturation.
$\theta$	the volumetric water content.
$\theta_r$	the residual water contents.
$egin{aligned} eta_s \ eta_i \end{aligned}$	the maximum volumetric water content. the soil initial moisture content.
$\sigma_i$	
$\sigma_n$	the soil column normal stress, $kg/(m s^2)$ .
$ au_h$	the shear strength, $kg/(m s^2)$ .
$ au_R$	the residual soil strength after failure at the sliding surface, $kg/(m s^2)$ .
$ au_{ m rf}$	the shear stress of slope runoff, $kg/(m s^2)$ .
$ au_{ ext{rs,z}}$	the shear strength (as a function of depth) provided by roots, $kg/(m s^2)$ .
$ au_s$	the shear stress, $kg/(m s^2)$ .
$ au_T$	the stress from the upslope columns or downslope columns when the soil column is unsta-
	ble, $kg/(m s^2)$ .
$T_R$	the experimentally measured root tensile strength, $kg/(m s^2)$ .
$w_{ m seep}$	the water volume lost via seepage in step $i$ , m.
W	the downslope force component of the soil column on the slip interface, $kg/(m s^2)$ .
$W_d$	the total sliding force of the soil column on the slip surface, $kg/(m s^2)$ .
$W_{r,i}$	the water of input the reservoir of ground water in step $i$ , m.
$\gamma_w$	the bulk densities of the water and soil minerals, kg m <sup>-3</sup> .
$\gamma_r$	the bulk densities of the soil minerals, kg m <sup>-3</sup> .
Z	the soil depth, m.
$Z_d$	the depth of the wetting front, m.

#### **Conflict of Interest**

The authors declare no conflicts of interest relevant to this study.

#### Acknowledgments

This research work was supported by the Science and Technology Research Program of Institute of Mountain Hazards and Environment, Chinese Academy of Sciences, the Strategic Priority Research Program of the Chinese Academy of Sciences (XDA23090202), International Science & Technology Cooperation Program of China (2018YFE0100100) and the National Natural Science Foundation of China (Grants 42172320 and 41877524). The manuscript benefited from the insightful comments by the three anonymous reviewers.

## **Data Availability Statement**

The data used to generate the figures in this study can be found in (Hu, 2023).

#### References

Aleotti, P. (2004). A warning system for rainfall-induced shallow failures. Engineering Geology, 73(3–4), 247–265. https://doi.org/10.1016/j.enggeo.2004.01.007

Arnold, J. G., Kiniry, J. R., Srinivasan, R., Williams, J. R., Haney, E. B., & Neitsch, S. L. (2012). Soil and water assessment tool input/output file documentation: Version 2012. Texas Water Resources Institute. TR 436. Retrieved from http://swatmodel.tamu.edu/documentation/

Arnone, E., Noto, L. V., Lepore, C., & Bras, R. L. (2011). Physically-based and distributed approach to analyze rainfall-triggered landslides at watershed scale. *Geomorphology*, 133(3–4), 121–131. https://doi.org/10.1016/j.geomorph.2011.03.019

Bagwari, S., Gehlot, A., Singh, R., Priyadarshi, N., & Khan, B. (2021). "Low-cost sensor-based and LoRaWAN opportunities for landslide monitoring systems on IoT platform: A review". *IEEE Access*, 10, 7107–7127. https://doi.org/10.1109/ACCESS.2021.3137841

JIANG ET AL. 22 of 25



- Bak, P., Tang, C., & Wiesenfeld, K. (1988). Self-organized criticality. *Physical Review A*, 38(1), 364–374. https://doi.org/10.1103/PhysRevA.38.364
  Baum, R., Savage, W., & Godt, J. (2002). TRIGRS-A FORTRAN program for transient rainfall infiltration and grid-based regional slope-stability analysis. *U.S. Geological Survey*. Open File Report 02–0424. https://doi.org/10.3133/ofr02424
- Bellugi, D., Milledge, D. G., Dietrich, W. E., McKean, J. A., Perron, J. T., Sudderth, E. B., & Kazian, B. (2015). A spectral clustering search algorithm for predicting shallow landslide size and location. *Journal of Geophysical Research: Earth Surface*, 120(2), 300–324. https://doi.org/10.1002/2014JF003137
- Bellugi, D., Milledge, D. G., Dietrich, W. E., Perron, J. T., & McKean, J. (2015). Predicting shallow landslide size and location across a natural landscape: Application of a spectral clustering search algorithm. *Journal of Geophysical Research: Earth Surface*, 120(12), 2552–2585. https://doi.org/10.1002/2015JF003520
- Bellugi, D. G., Milledge, D. G., Cuffey, K. M., Dietrich, W. E., & Larsen, L. G. (2021). Controls on the size distributions of shallow landslides. Proceedings of the National Academy of Sciences of the United States of America, 118(9). https://doi.org/10.1073/pnas.2021855118
- Bishop, A. W. (1960). The principle of effective stress. Norwegian Geotechnical Institute, 32, 1-5.
- Borga, M., DallaFontana, G., Gregoretti, C., & Marchi, L. (2002). Assessment of shallow landsliding by using a physically based model of hillslope stability. *Hydrological Processes*, 16(14), 2833–2851. https://doi.org/10.1002/hyp.1074
- Bout, B., Lombardo, L., Van Westen, C. J., & Jetten, V. (2018). Integration of two-phase solid fluid equations in a catchment model for flashfloods, debris flows and shallow slope failures. *Environmental Modelling & Software*, 105(Jul), 1–16. https://doi.org/10.1016/j.envsoft.2018.03.017
- Brand, E. W. (1984). Landslides in Southeast Asia: A state-of-art report. In *Proceedings of 4th International Symposium on landslides* (pp. 17–59). Canadian Geotechnical Society.
- Brand, E. W. (1992). Keynote paper: Slope instability in tropical areas. In D. H. Bell (Ed.), *Proceedings of 6th International Symposium on landslides* (pp. 2031–2051). Balkema.
- Brooks, R. J., & Corey, A. T. (1964). Hydraulic properties of porous media, Hydrology paper 3. Colorado State University.
- Burton, A., & Bathurst, T. J. (1998). Physically based modeling of shallow landslides sediment yield at the catchment scale. *Environmental Geology*, 35(2–3), 89–99. https://doi.org/10.1007/s002540050296
- Caine, N. (1980). The rainfall intensity-duration control of shallow landslides and debris flows. *Geografiska Annaler, Series A*, 62(1/2), 23–27. https://doi.org/10.2307/520449
- Camporese, M., Paniconi, C., Putti, M., & Orlandini, S. (2010). Surface-subsurface flow modeling with path-based runoff routing, boundary condition-based coupling, and assimilation of multisource observation data. Water Resources Research, 46(2). https://doi.org/10.1029/2008WR007536
- Casadei, M., Dietrich, W., & Miller, N. (2003). Testing a model for predicting the timing and location of shallow landslides initiation in soil-mantled landscapes. Earth Surface Processes and Landforms, 28(9), 925–950. https://doi.org/10.1002/esp.470
- Chen, L., & Young, M. H. (2006). Green-Ampt infiltration model for sloping surfaces. Water Resources Research, 42(7), W07420. https://doi.org/10.1029/2005WR004468
- Chen, W., Nover, D., Yen, H., Xia, Y., He, B., Sun, W., & Viers, J. (2020). Exploring the multi-scale hydrologic regulation of multi-pond systems in a humid agricultural catchment. Water Research, 184, 115987. https://doi.org/10.1016/j.watres.2020.115987
- Chen, W. L., Du, J., Fang, Y. C., Wang, D. J., He, S. T., Lan, H. J., & Zhao, P. (2019). Soil reinforcement effect of root systems of typical plants in areas with frequent debris flow. *Bulletin of Soil and Water Conservation*, 39(5), 32–39. (In Chinese). https://doi.org/10.13961/j.cnki. stbcth 2019.05.005
- Crosta, G. B. (1998). Regionalization of rainfall thresholds: An aid to landslides hazard evaluation. *Environmental Geology*, 35(2–3), 131–145. https://doi.org/10.1007/s002540050300
- Dietrich, W. E., & Montgomery, D. R. (1998). SHALSTAB: A digital terrain model for mapping shallow landslides potential. NCASI (National Council of the Paper Industry for Air and Stream Improvement) Technical Report (p. 29).
- Faillettaz, J., Sornette, D., & Funk, M. (2011). Numerical modeling of a gravity-driven instability of a cold hanging glacier: Reanalysis of the 1895 break-off of Altelsgletscher, Switzerland. *Journal of Glaciology*, 57(205), 817–831. https://doi.org/10.3189/002214311798043852
- Fan, L., Lehmann, P., & Or, D. (2015). Effects of hydromechanical loading history and antecedent soil mechanical damage on shallow landslides triggering. *Journal of Geophysical Research: Earth Surface*, 120(10), 1990–2015. https://doi.org/10.1002/2015JF003615
- Fan, L., Lehmann, P., Zheng, C., & Or, D. (2020). Rainfall intensity temporal patterns affect shallow landslides triggering and hazard evolution. Geophysical Research Letters, 47(1), e2019GL085994. https://doi.org/10.1029/2019GL085994
- Fan, L. F., Lehmann, P., Mcardell, B., & Or, D. (2017). Linking rainfall-induced landslides with debris flows runout patterns towards catchment scale hazard assessment. *Geomorphology*, 280(1), 1–15. https://doi.org/10.1016/j.geomorph.2016.10.007
- Fan, L. F., Lehmann, P., & Or, D. (2016). Effects of soil spatial variability at the hillslope and catchment scales on characteristics of rainfall-induced landslides. *Water Resources Research*, 52(3), 1781–1799. https://doi.org/10.1002/2015WR017758
- Fan, L. F., Lehmann, P., & Or, D. (2017). Load redistribution rules for progressive failure in shallow landslides: Threshold mechanical models. Geophysical Research Letters, 44(1), 228–235. https://doi.org/10.1002/2016GL071763
- Formetta, G., Simoni, S., Godt, J. W., Lu, N., & Rigon, R. (2016). Geomorphological control on variably saturated hillslope hydrology and slope instability. Water Resources Research, 52(6), 4590–4607. https://doi.org/10.1002/2015WR017626
- Godt, J. W., Baum, R. L., Savage, W. Z., Salciarini, D., Schulz, W. H., & Harp, E. L. (2008). Transient deterministic shallow landslides modeling: Requirements for susceptibility and hazard assessments in a GIS framework. *Engineering Geology*, 102(3-4), 214–226. https://doi.org/10.1016/j.enggeo.2008.03.019
- Godt, J. W., Sener-Kaya, B., Lu, N., & Baum, R. L. (2012). Stability of infinite slopes under transient partially saturated seepage conditions. Water Resources Research, 48(5), W05505. https://doi.org/10.1029/2011WR011408
- Goodman, R. E. (1980). Introduction to rock mechanics. John Wiley. (xii +, p. 478). https://doi.org/10.1016/0013-7952(82)90015-1
- Guo, X. J., Cui, P., & Yong, L. I. (2013). Debris flow warning threshold based on antecedent rainfall: A case study in Jiangjia Ravine, Yunnan, China. *Journal of Mountain Science*, 10(2), 305–314. https://doi.org/10.1007/s11629-013-2521-z
- Guo, X. J., Li, Y., Cui, P., Yan, H., & Zhuang, J. (2020). Intermittent viscous debris flow formation in Jiangjia Gully from the perspectives of hydrological processes and material supply. *Journal of Hydrology*, 589, 125184. https://doi.org/10.1016/j.jhydrol.2020.125184
- Guzzetti, F., Peruccacci, S., Rossi, M., & Stark, C. P. (2007). Rainfall thresholds for the initiation of landslides in central and southern Europe. Meteorology and Atmospheric Physics, 98(3-4), 239-267. https://doi.org/10.1007/s00703-007-0262-7
- Guzzetti, F., Peruccacci, S., Rossi, M., & Stark, C. P. (2008). The rainfall intensity–duration control of shallow landslides and debris flows: An update. *Landslides*, 5(1), 3–17. https://doi.org/10.1007/s10346-007-0112-1
- Hengl, T., Mendesde Jesus, J., Heuvelink, G. B., Ruiperez Gonzalez, M., Kilibarda, M., Blagotic, A., et al. (2017). SoilGrids250m: Global grid-ded soil information based on machine learning. PLoS One, 12(2), e0169748. https://doi.org/10.1371/journal.pone.0169748

JIANG ET AL. 23 of 25



- Hergarten, S., & Neugebauer, H. J. (2000). Self-organized criticality in two-variable models. *Physical Review E Statistical Physics, Plasmas, Fluids, and Related Interdisciplinary Topics*, 61(3), 2382–2385. https://doi.org/10.1103/PhysRevE.61.2382
- Hu, M. J., Ren, W., & Jianhua, S. (2011). Rainfall landslides and debris flow intergrowth relationship in Jiangjia Ravine. *Journal of Mountain Science*, 8(004), 603–610. https://doi.org/10.1007/s11629-011-2131-6
- Hu, X. (2023). A physically based model for the sequential evolution analysis of rainfall-induced shallow landslides in a catchment. [Dataset]. https://doi.org/10.5281/zenodo.7529382
- Iverson, R. M. (1997). The physics of debris flows. Reviews of Geophysics, 35(3), 245-296. https://doi.org/10.1029/97RG00426
- Iverson, R. M. (2000). Landslide triggering by rain infiltration. Water Resources Research, 36(7), 1897–1910. https://doi.org/10.1029/2000WR900090
- Jemec, M., & Komac, M. (2013). Rainfall patterns for shallow landsliding in perialpine Slovenia. Natural Hazards, 67(3), 1011–1023. https://doi.org/10.1007/s11069-011-9882-9
- Jonathan, W., Godt, R. L. B., & Chleborad, A. F. (2006). Rainfall characteristics for shallow landsliding in Seattle, Washington, USA. Earth Surface Processes and Landforms, 31(1), 97–110. https://doi.org/10.1002/esp.1237
- Kuriakose, S. L., Beek, L., & Westen, C. (2010). Parameterizing a physically based shallow landslide model in a data poor region. Earth Surface Processes and Landforms, 34(6), 867–881. https://doi.org/10.1002/esp.1794
- Larsen, M. C., & Simon, A. (1993). A rainfall intensity-duration threshold for landslides in a humid-tropical environment. Puerto Rico. Geografiska Annaler Series A, 75(1/2), 13–23. https://doi.org/10.2307/521049
- Lehmann, P., & Or, D. (2012). Hydromechanical triggering of landslides: From progressive local failures to mass release. Water Resources Research, 48(3), 3535–3558. https://doi.org/10.1029/2011WR010947
- Lu, N., & Godt, J. (2008). Infinite slope stability under steady unsaturated seepage conditions. Water Resource Research, 44(11), W11404. https://doi.org/10.1029/2008WR006976
- Lu, N., Şener-Kaya, B., Wayllace, A., & Godt, J. W. (2012). Analysis of rainfall-induced slope instability using a field of local factor of safety. Water Resources Research, 48(9). https://doi.org/10.1029/2012WR011830
- Ma, T., Li, C., Lu, Z., & Wang, B. (2014). An effective antecedent precipitation model derived from the power-law relationship between land-slides occurrence and rainfall level. *Geomorphology*, 216(Jul.1), 187–192. https://doi.org/10.1016/j.geomorph.2014.03.033
- Maharjan, G. R., Park, Y. S., Kim, N. W., Shin, D. S., Choi, J. W., Hyun, G. W., et al. (2013). Evaluation of SWAT sub-daily runoff estimation at small agricultural watershed in Korea. Frontiers of Environmental Science & Engineering, 7(1), 109–119. https://doi.org/10.1007/s11783-012-0418-7
- Malet, J. P., Van Asch, T. W., Van Beek, R., & Maquaire, O. (2005). Forecasting the behaviour of complex landslides with a spatially distributed hydrological model. Natural Hazards and Earth System Sciences, 5(1), 71–85. https://doi.org/10.5194/nhess-5-71-2005
- Matsushi, Y., & Matsukura, Y. (2006). Cohesion of unsaturated residual soils as a function of volumetric water content. *Bulletin of Engineering Geology and the Environment*, 65(4), 449–455. https://doi.org/10.1007/s10064-005-0035-9
- Mehan, S., Neupane, R. P., & Kumar, S. (2017). Coupling of SUFI 2 and SWAT for improving the simulation of streamflow in an agricultural watershed of South Dakota. *Journal of Waste Water Treatment & Analysis*, 08(03). https://doi.org/10.4172/2157-7587.1000280
- Mein, R. G., & Larson, C. L. (1973). Modeling infiltration during a steady rain. Water Resource Research, 9(2), 384–394. https://doi.org/10.1029/WR009i002p00384
- Moonhyun, H., Sangseom, J., & Jaehong, K. (2019). A combined method for modeling the triggering and propagation of debris flows. *Landslides*, 17(2), 805–824. https://doi.org/10.1007/s10346-019-01294-5
- Morrissey, M. M., Wieczorek, G. F., & Morgan, B. A. (2008). A comparative analysis of simulated and observed landslides locations triggered by Hurricane Camille in Nelson County, Virginia. *Hydrological Processes*, 22(4), 524–531. https://doi.org/10.1002/hyp.6882
- Mouazen, A. M., Ramon, H., & De Baerdemaeker, J. (2002). SW-soil and water: Effects of bulk density and moisture content on selected mechanical properties of sandy loam soil. *Biosystems Engineering*, 83(2), 217–224. https://doi.org/10.1006/bioe.2002.0103
- Mullins, C. E., & Panayiotopoulos, K. P. (1984). The strength of unsaturated mixtures of sand and kaolin and the concept of effective stress. Journal of Soil Science, 35(3), 459–468. https://doi.org/10.1111/j.1365-2389.1984.tb00303.x
- Netto, A. L. C., Sato, A. M., Avelar, A. S., Vianna, L. G. G., Araújo, I. S., Ferreira, D. L. C., et al. (2011). January 2011: The extreme landslides disaster in Brazil. *Proceedings of the Second World Landslides Forum.* 3–7(October 2011), 1–6.
- Pack, R. T., Tarboton, D. G., & Goodwin, C. N. (1998). SINMAP, A stability index approach to terrain stability hazard mapping. In SINMAP
- user's manual (Vol. 68). Terratech Consulting Ltd.
  Perla, R., Cheng, T. R., & McClung, D. M. (1980). A two-parameter model of snow-avalanche motion. Journal of Glaciology, 26(94), 197–207.
- https://doi.org/10.3189/S002214300001073X
  Piegari, E., Cataudella, V., Di Maio, R., Milano, L., & Nicodemi, M. (2006). A cellular automaton for the factor of safety field in landslides modeling. *Geophysical Research Letters*, 1(33), L01403. https://doi.org/10.1029/2005GL024759
- Pollen, N., & Simon, A. (2005). Estimating the mechanical effects of riparian vegetation on stream bank stability using a fiber bundle model. Water Resources Research, 41(7), 226–244. https://doi.org/10.1029/2004WR003801
- Preti, F. (2006). On the root reinforcement modeling.  $Geophysical\ Research\ Abstracts,\ 8,\ 4555.$
- Rahardjo, H., Ong, T. H., Rezaur, R. B., & Leong, E. C. (2007). Factors controlling instability of homogeneous soil slopes under rainfall. *Journal of Geotechnical & Geoenvironmental Engineering*, 133(12), 1532–1543. https://doi.org/10.1061/(ASCE)1090-0241
- Rahimi, A., Rahardjo, H., & Leong, E. C. (2011). Effect of antecedent rainfall patterns on rainfall-induced slope failure. *Journal of Geotechnical and Geoenvironmental Engineering*, 137(5), 483–491. https://doi.org/10.1061/(ASCE)GT.1943-5606.0000451
- Rawls, W. J., Brakensiek, D. L., & Saxton, K. E. (1982). Estimation of soil water properties. Transactions of the American Society Agricultural Engineering, 25(5), 1316–1320. https://doi.org/10.13031/2013.33720
- Rigon, R., Bertoldi, G., & Over, T. M. (2006). GEOtop: A distributed hydrological model with coupled water and energy budgets. *Journal of Hydrometeorology*, 7(3), 371–388. https://doi.org/10.1175/JHM497.1
- Schmidt, K. M., Roering, J. J., Stock, J. D., Dietrich, W. E., Montgomery, D. R., & Schaub, T. (2001). The variability of root cohesion as an influence on shallow landslides susceptibility in the Oregon Coast Range. *Canadian Geotechnical Journal*, 38(5), 995–1024. https://doi.org/10.1139/t01-031
- Schwarz, M., Preti, F., Lehmann, P., & Or, D. (2010). Quantifying the role of vegetation in slope stability: A case study in Tuscany (Italy). Ecological Engineering, 36(3), 285–291. https://doi.org/10.1016/j.ecoleng.2009.06.014
- Segoni, S., Piciullo, L., & Gariano, S. L. (2018). A review of the recent literature on rainfall thresholds for landslides occurrence. *Landslides*, 15(8), 1483–1501. https://doi.org/10.1007/s10346-018-0966-4
- Shen, P., Zhang, L., Chen, H., & Fan, R. (2018). EDDA 2.0: Integrated simulation of debris flow initiation and dynamics considering two initiation mechanisms. Geoscientific Model Development, 11(7), 2841–2856. https://doi.org/10.5194/gmd-11-2841-2018

JIANG ET AL. 24 of 25



- Sidle, R. C., & Ochiai, H. (2006). Landslides: Processes, prediction and land use. American Geophysical Union.
- Šimůnek, J., Genuchten, M. T., & Šejna, M. (2016). Recent developments and applications of the HYDRUS computer software packages. *Vadose Zone Journal*, 15(7), 1–25. https://doi.org/10.2136/vzj2016.04.0033
- Subramanian, S. S., Fan, X., Yunus, A. P., van Asch, T., Scaringi, G., Xu, Q., et al. (2020). A sequentially coupled catchment-scale numerical model for snowmelt-induced soil slope instabilities. *Journal of Geophysical Research: Earth Surface*, 125, e2019JF005468. https://doi.org/10.1029/2019JF005468
- Swanson, F. J., & Swanston, D. N. (1976). Complex mass-movement terrains in the Western cascade range. *Oregon Review Engineering Geology*, 3 113–124
- Terlien, M. T. (1998). The determination of statistical and deterministic hydrological landslides-triggering thresholds. *Environmental Geology*, 35(2–3), 124–130. https://doi.org/10.1007/s002540050299
- Tian, X. F., Li, Y., & Tian, Q. Y. (2021). Potential sediment sources identification of debris flows in the Jiangjia Gully, China. *Journal of Mountain Science*, 18(7), 1886–1901. https://doi.org/10.1007/s11629-019-5787-y
- Vanapalli, S. K., Fredlund, D. G., Pufahl, D. E., & Clifton, A. W. (1996). Model for the prediction of shear strength with respect to soil suction. Canadian Geotechnical Journal, 33(3), 379–392. https://doi.org/10.1139/t96-060
- Von Ruette, J., Lehmann, P., & Or, D. (2013). Rainfall-triggered shallow landslides at catchment scale: Threshold mechanics-based modeling for abruptness and localization. Water Resources Research, 49(10), 6266–6285. https://doi.org/10.1002/wrcr.20418
- Von Ruette, J., Lehmann, P., & Or, D. (2014). Effects of rainfall spatial variability and intermittency on shallow landslides triggering patterns at a catchment scale. Water Resources Research, 50(10), 7780–7799. https://doi.org/10.1002/2013WR015122
- Waldron, L. J. (1977). The shear resistance of root-permeated homogenous and stratified soil. *Journal of the Soil Science Society of America*, 41(5), 843–849. https://doi.org/10.2136/sssaj1977.03615995004100050005x
- Wang, Y. Y., Jan, Q. D., Yong, H., & Tian, B. (2009). Analysis of rheological characteristics of soil in source area of debris flow to answer process to rainfall. *Journal of Mountain Science*, 27(4), 457–465. (in Chinese).
- Woldemeskel, F., & Sharma, A. (2016). Should flood regimes change in a warming climate? The role of antecedent moisture conditions. Geophysical Research Letters, 43(14), 7556–7563. https://doi.org/10.1002/2016GL069448
- Wu, T. H., Mckinnell, W. P., & Swanston, D. N. (1979). Strength of tree roots and landslides on Prince of Wales Island, Alaska. Canadian Geotechnical Journal, 35(4), 579–590. https://doi.org/10.1139/t79-003
- Wu, W., & Sidle, R. (1995). A distributed slope stability model for steep forested basins. Water Resources Research, 31(8), 2097–2110. https://doi.org/10.1029/95WR01136
- Yang, H., Yang, T., Zhang, S., Zhao, F., Hu, K., & Jiang, Y. (2020). Rainfall-induced landslides and debris flows in Mengdong Town, Yunnan Province, China. *Landslides*, 17(4), 931–941. https://doi.org/10.1007/s10346-019-01336-y
- Zhang, S. J., Xu, C. X., Wei, F. Q., Hu, K., Xu, H., Zhao, L., & Zhang, G. (2019). A physics-based model to derive rainfall intensity-duration threshold for debris flow. *Geomorphology*, 351, 106930. https://doi.org/10.1016/j.geomorph.2019.106930
- Zhuang, J. Q., Peng, C., Wang, G., Chen, X., Iqbal, J., & Guo, X. (2015). Rainfall thresholds for the occurrence of debris flows in the Jiangjia Gully, Yunnan Province, China. *Engineering Geology*, 195, 335–346. https://doi.org/10.1016/j.enggeo.2015.06.006

JIANG ET AL. 25 of 25